HIGH THROUGHPUT PLATFORM FOR MULTISCALE QUANTITATIVE PHASE IMAGING

BY

MIKHAIL KANDEL

THESIS

Submitted in partial fulfillment of the requirements
for the degree of Master of Science in Electrical and Computer Engineering
in the Graduate College of the
University of Illinois at Urbana-Champaign, 2016

Urbana, Illinois

Adviser:

Associate Professor Gabriel Popescu

ABSTRACT

Quantitative phase imaging (QPI) yields the spatial phase map of the object's scattering potential. QPI has enabled unprecedented label-free studies in biomedicine, ranging from cell dynamics and growth to cancer diagnosis and prognosis. The field is currently transitioning from technology-driven to application-driven research and from engineering-background users to biomedical-background users. Aligned with these efforts, we present our recent advances in high-throughput, user-friendly QPI technology for multiscale spatiotemporal imaging.

TABLE OF CONTENTS

LIST OF ACRONYMS

DIC   Differential Interference Contrast

DPM   Diffraction Phase Microscopy

DPS   Dispersion Phase Spectroscopy

GLIM   Gradient Light Interference Microscopy

PC   Phase Contrast

QPI   Quantitative Phase Imaging

SLM   Spatial Light Modulator

SLIM   Spatial Light Interference Microscopy

CHAPTER 1: INTRODUCTION

Biological microstructures do not absorb visible light in appreciable quantities. Thus, label-free contrast enhancement techniques must use interferometric methods to couple phase information into observable intensity modulation. Although techniques such as phase contrast or differential interference contrast are mainstays of traditional microscopy [1, 2], the image recorded on the camera is "qualitative" in the sense that it is not linearly related to the object's internal structure, often containing significant artifacts. To improve upon these methods, quantitative phase imaging techniques aim to recover structural information by measuring the precise optical pathlength shift introduced by the object's scattering potential (Chapter 1). Over the last decade these methods have found applications in hematology [3-8], cellular physiology [9-21], studies of population growth [22-29], along with clinical applications [30-35].

Nevertheless, typical quantitative phase imaging systems (such as those described in Chapter 2) were cumbersome to use, imposing practical limits on the complexity of an experiment with little hope of use by a person without an engineering background. In this research, we focus on advancing QPI methods by making them easy to use and high-throughput via new instrumentation and software tools.

To this end, we concentrated on removing the barriers for phase imaging by developing high-throughput systems capable of conducting experiments at all biologically relevant scales. Specifically, we developed a multiscale imaging platform that seamlessly transitions between transmitted light imaging and fluorescent microscopy (Chapter 3) [33]. With these new capabilities, we were able to study, with the same tool, the dynamics of cellular populations as well as nanometer size structures that are part of the cellular skeleton (Chapter 4) [36-38]. With higher throughput systems, we proposed an approach for tomographic reconstruction that can be used to visualize intracellular transport, along with a new QPI modality designed for imaging thick structures (Chapter 5). Lastly, we describe a design for an image

processing pipeline to digitize and process clinically prepared pathology slides, which, to the best of our knowledge is the first dedicated quantitative phase tissue scanning instrument (Chapter 6) [39-43].

The resulting systems are scheduled to be deployed at the Beckman Institute for Advanced Science and Technology at the University of Illinois at Urbana-Champaign as part of a shared facility for campus-wide use.

CHAPTER 2: IMAGE FORMATION

2.1 Interferometric Microscopy

The phase shift introduced by a sample under broadband illumination can be understood as the argument of the temporal cross-correlation function between a reference and a sample-perturbed field (Figure 1).

Owing to the high frequencies typical of the optical regime, conventional detectors average many optical cycles during a single exposure [44]. Thus, we understand the signal recorded on the detector as an average intensity:

$$I = \left\langle U^*(t)U(t) \right\rangle_t \tag{1}$$

where angular brackets denote a temporal average.

In the case of a thin transparent sample, with transmission function (T), under plane wave illumination ($e^{i\beta_o z}$, $\beta_0 = \omega/c$), the intensity at the detector is insensitive to sample information (Figure 1):

$$T = e^{i\theta} \quad U = Te^{i\beta_o z}$$
$$I = \left\langle U^*(t)U(t) \right\rangle_t = 1 \tag{2}$$
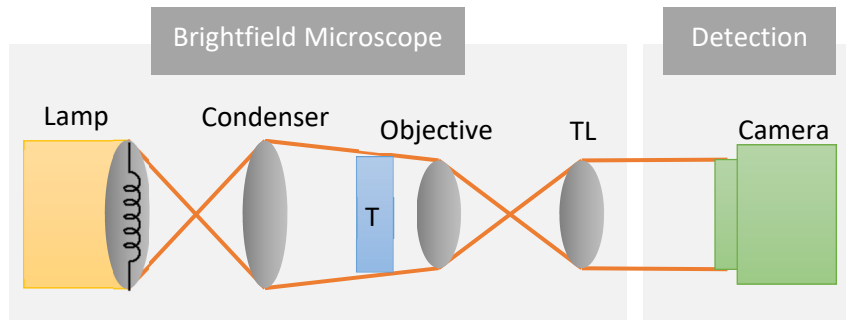
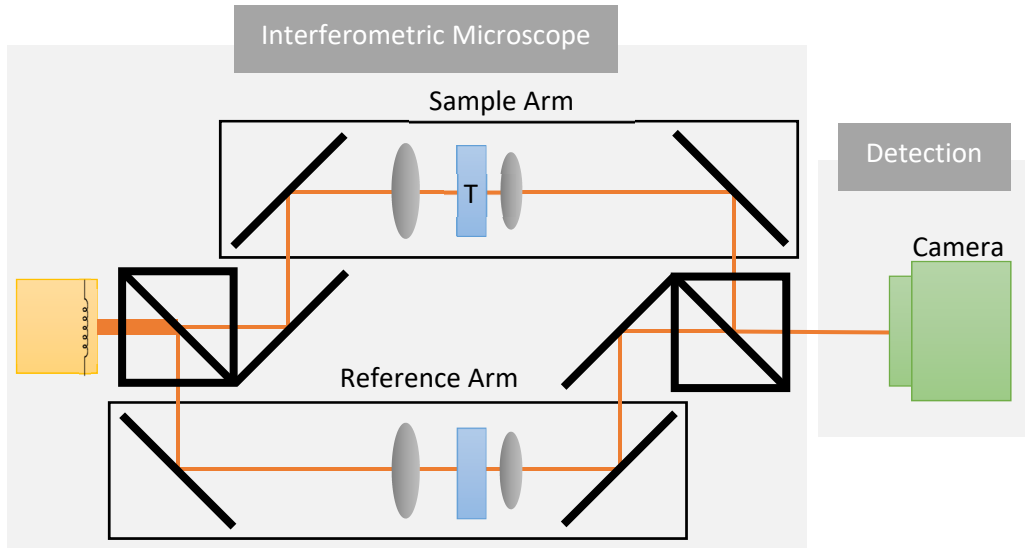**Figure 1: Brightfield microscope.** The condenser focuses down the illumination onto the sample (*T*). The light is then collected by the objective and transported through infinity corrected optics to the camera (TL, tube lens). Although this system has poor sensitivity to phase information, it remains popular for clinical applications, such as H&E staining, where contrast is generated from amplitude information [45].

With the introduction of a second wavefront, the phase information couples into detectable intensity information (Figure 2):

$$I(\tau) = \left\langle \left| U_0(t) + U_1(t+\tau) \right|^2 \right\rangle_t$$
$$= \left\langle \left| U_0(t) \right|^2 \right\rangle_t + \left\langle \left| U_1(t+\tau) \right|^2 \right\rangle_t + \left\langle \left| U_0(t) \right|^* \left| U_1(t+\tau) \right| \right\rangle_t + c.c. \qquad (3)$$

Thus, under broadband illumination, the contrast forming quantity in QPI, a radian value at each pixel, is understood as the argument of the spatial-temporal autocorrelation at zero lag. Typically, this is the argument of the phase at the central wavelength [46].

$$U_1 = U_0 T = U_0 e^{i\theta}$$
$$\Gamma_{1,2} \triangleq \left\langle \left| U_0(t) \right|^* \left| U_1(t+\tau) \right| \right\rangle_t \qquad (4)$$
$$I(\tau) = I_1 + I_0 + 2\text{Re}\left[\Gamma(\tau) e^{i\theta} \right]$$

Figure 2: A Mach–Zehnder type microscope. Interferometric contrast is generated by the coherent addition of a sample perturbed field with an unperturbed reference. In a typical implementation, the setup contains two identical optical paths, each with a separate condenser and objective. During imaging, a matching sample is placed at the reference arm to compensate for dispersion. Such systems were once popular for studies of biological specimen [46-48], and today, with modifications, this design is typically used for surface inspection in manufacturing processes [49]. The ray tracing diagrams are omitted for clarity.

Due to mechanical instability, it is challenging to construct a Mach-Zehnder interferometer for high-resolution widefield imaging of biological samples. Further, such a system would be difficult to combine with existing microscopes. To achieve stability, a reference field can be generated by spatially filtering the sample field (Figure 3). This a "common-path interferometer" [50], achieves a narrow spatial filter function ($\widetilde{H}(k_x, k_y) = \Im\{H(x,y)\}$) so that the reference field maintains a constant value over the entirety of the field of view [51, 52]:

$$I(x,y) = |U_1 + U_2|^2 = |(H \otimes T)U_0 + TU_0|^2 = |aU_0 + TU_0|^2$$
$$I = I_1 + I_2 + 2aI_0 \cos\theta \tag{5}$$

where $a = H \otimes U_0$, which approaches a constant complex field, as $\widetilde{H}(k_x, k_y)$ approaches a delta function. I_0 is the incident intensity.

In a typical QPI system, the interference term is isolated from the intensity background contributions ($I_1 + I_2$) using either phase shifting (temporal modulation) or off-axis approaches (spatial modulation). In SLIM, phase shifting is achieved using a liquid crystal based spatial light modulator [53]. DPM, an off-axis, common-path technique, employs a diffraction grating as a beam splitter [54].

The irradiance registered on the detector is digitally post-processed to yield a per-pixel value of the phase.
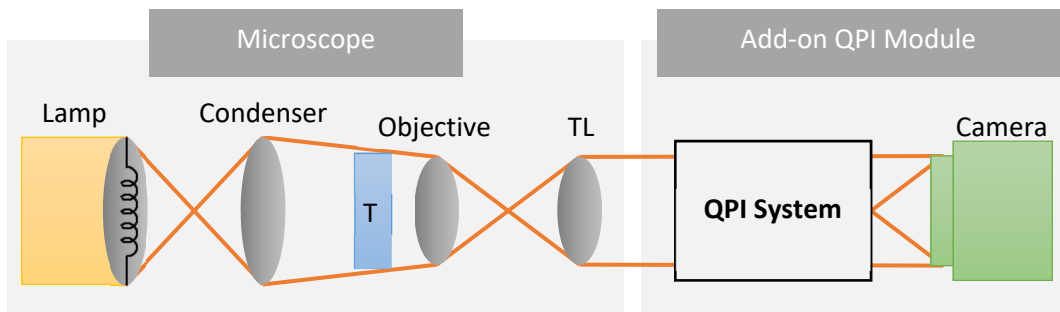
Figure 3: A common-path interferometric microscope. A spatial filter generates a reference beam from the sample perturbed field. Thus, the system is "self-referenced" and can be attached to the output port of a conventional microscope. The design, operation, and applications for the "QPI Module " is the subject of this thesis.

2.2 Quantitative Phase Imaging Systems

2.2.1 Diffraction Phase Microscopy: Off-Axis, Common-Path

In Diffraction Phase Microscopy (DPM, Figure 4) [54-56], a phase grating is used to split the sample perturbed-field into diffraction orders (0 and ±1), followed by the generation of the reference field through the use of a pinhole (P), which describes the function (H), in the previous section.

Thus, the field at the camera can be expressed as:

$$U(x,y) = U_1 + U_2(x,y)e^{i\alpha x} \tag{6}$$

where $\alpha = 2\pi/\Lambda$ and $U_1 = (U_0 t) \otimes H$ is a constant, and Λ is the period of the grating.

The detected intensity has the form:

$$I(x,y) = I_1 + I_2(x,y) + 2\sqrt{I_1 I_2(x,y)}\cos[\phi(x,y) - \alpha x], \tag{7}$$

where ϕ is the measured phase. With a sufficiently high grating frequency (α), the amplitude image is separated from the modulation in the frequency domain (Figure 4). See ref. [57] for details on sampling conditions in DPM. The phase is obtained from the argument of the analytic signal taken at the frequency of the grating. This signal is obtained via a Hilbert transform, which is equivalent to selecting one order in the frequency domain and performing an inverse Fourier transform. The resulting phase map is unique when taken relative to a background measurement of a sample free region. The resulting Fourier transform of the measured intensity is:

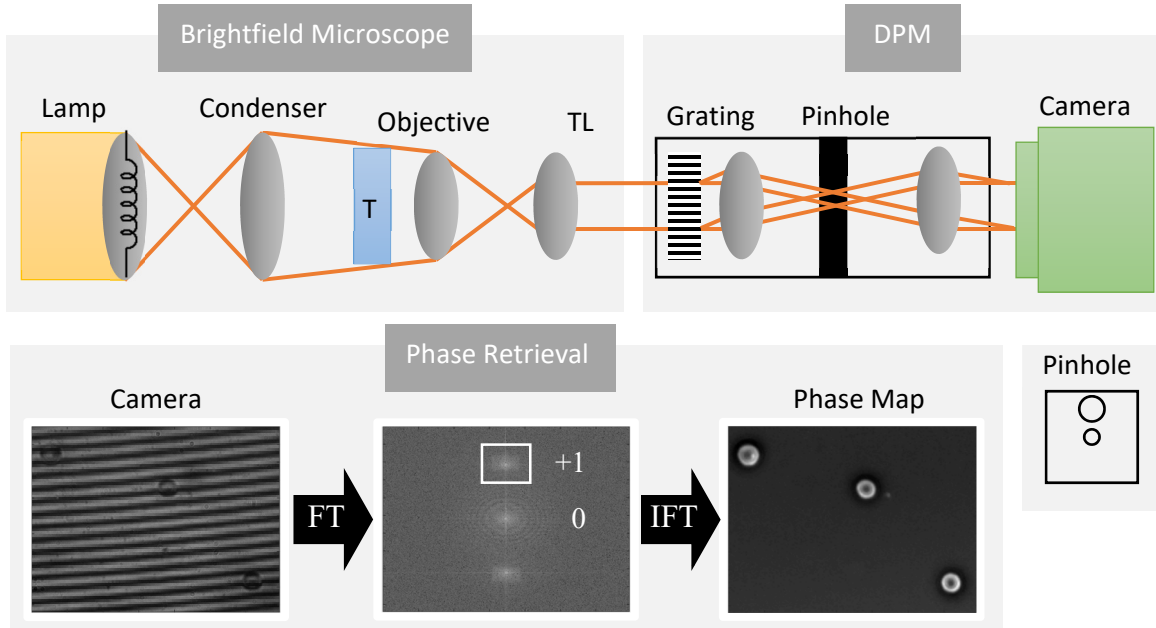$$\tilde{I}_{FT}(k_x, k_y) = \tilde{I}_0 + \tilde{I}_0 \otimes [d(k_x - \alpha) + d(k_x + \alpha)](k_x, k_y) \tag{8}$$

The cropped region contains only the first order:

$$\tilde{I}_C = [\tilde{I}_0 d(k_x - \alpha)]_{crop} \tag{9}$$

Taking the inverse Fourier transform, the measured phase reads:

6

$$\phi(x,y) = \arg\left(I_{C\_sample}(x,y) \Big/ I_{C\_background}(x,y)\right) \tag{10}$$

where $I_{C\_background}$ comes from a sample-free image, acquired once per experiment.

Figure 4: DPM geometry. A diffraction grating is used to separate the phase from amplitude contributions. The resulting signal can be digitally demodulated in the spatial frequency domain. The system is typically attached to the output port of a microscope operating under brightfield illumination.

2.2.2 Spatial Light Interference Microscopy

While DPM-type interferometers are comparably inexpensive and acquire phase maps from a single snapshot, the resulting image suffers from a much lower space-bandwidth product [56-58]. Further, as the image is encoded in high spatial frequencies, even small vibrations in the spatial components ("twists") can lead to significant defects. The loss of light through the diffraction grating makes simultaneous fluorescence imaging impractical.

To build a compromise-free system, we turn to phase shifting interferometry and Spatial Light Interference Microscopy (SLIM) [57]. In SLIM, the phase shift between scattered and transmitted light is modulated by way of a spatial light modulator (SLM) placed at an external pupil plane, matched to the phase ring inside the objective (Figure 4). The phase map is recovered from four interference images,

whose phase offset is cycled between 0 and $3\pi/2$ in $\pi/2$ increments (Figure 5, field contributions). The total phase of the field (ϕ) is obtained from the phase shift between scattered and transmitted fields (ϕ_{ac}):

$$U = U_{dc} + U_{ac} \exp\left[i\left(\theta_{ac} + \varepsilon\right)\right] \tag{11}$$

where ε is the phase shift introduced by the SLM. The measured intensity as a function of ε is

$$I = \left|U_{dc}\right|^2 + \left|U_{ac}\right|^2 + 2\left|U_{dc}\right|\left|U_{ac}\right|\cos\left(\theta_{ac} + \varepsilon\right) \tag{12}$$

As a result, θ_{ac} can be obtained as:

$$\theta_{ac} = \tan^{-1}\left[\frac{I_{-\pi/2} - I_{\pi/2}}{I_0 - I_\pi}\right] \tag{13}$$

Since the phase of interest is that of the full field [59, 60], (see Figure. 5):

$$U = U_{dc} + U_{ac}$$
$$\theta = \arg\left\{\frac{\left|U_{ac}\right|\sin\left(\theta_{ac}\right)}{\left|U_{dc}\right| + \left|U_{ac}\right|\cos\left(\theta_{ac}\right)}\right\} \tag{14}$$

Finally, the ratio of the two amplitudes can be extracted from the four measured frames by solving the equation:

$$\left|\frac{U_{ac}}{U_{dc}}\right| + \left|\frac{U_{dc}}{U_{ac}}\right| = \frac{I_0 + I_\pi + I_{-\pi/2} + I_{\pi/2}}{I_0 - I_\pi + I_{-\pi/2} - I_{\pi/2}} \cdot \frac{1}{\sin\left(\theta_{ac}\right) + \cos\left(\theta_{ac}\right)} \tag{15}$$
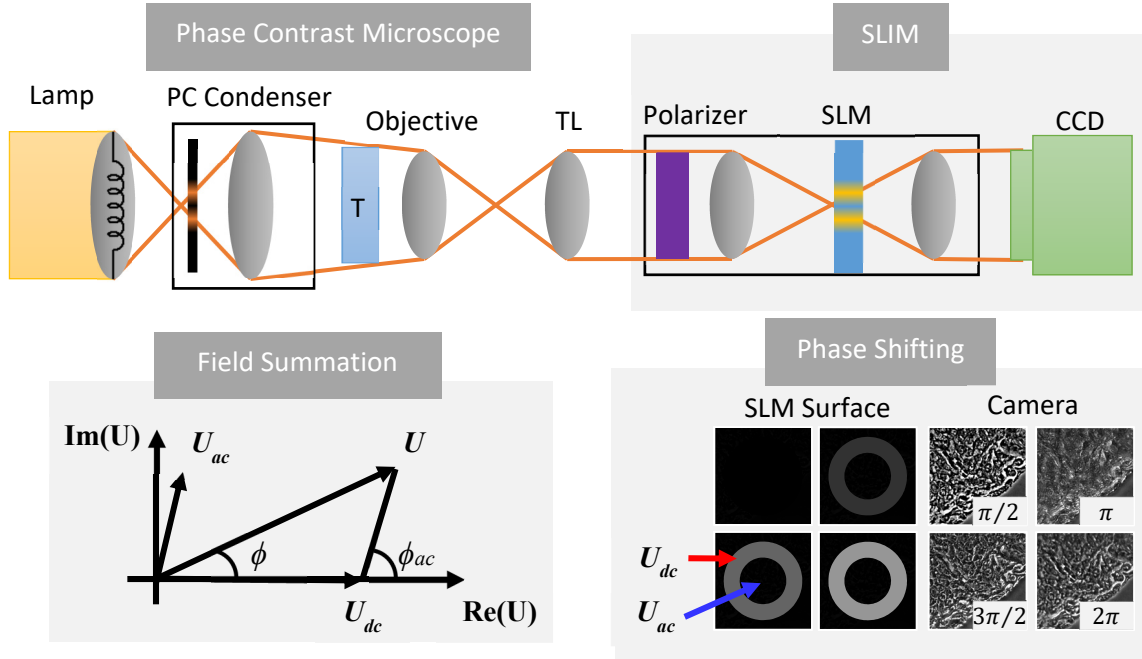
Figure 5: SLIM geometry. The total phase of the field (ϕ) is obtained from the phase shift between scattered and transmitted fields (ϕ_{ac}). When the system is placed at the output port of a phase contrast microscope, a flat pattern on the SLM corresponds to a $\pi/2$ offset between scattered and transmitted light. The phase can then be recovered by cycling the SLM, essentially modulating the phase ring matched to the low-frequency terms (U_{dc}). As indicated by the arrows, U_{ac} falls outside the phase ring.

2.2.3 Gradient Light Interference Microscopy

While the SLIM configuration provides exceptional sensitivity [61], the reference field is often significantly attenuated when going through a thick-specimen, such as a bovine embryo [62] or an acute brain slice [63]. To overcome these challenges, the contrast forming interference can be generated from laterally sheared beams — as is done in DIC (Figure 6).

The Jones matrix formulation that describes the system is as follows [64]:

$$\text{System} = \left(P_2\right)\left(\text{SLM}\right)\left(\text{NP}\right)\left(\text{Sample}\right)\left(\text{NP}\right)\left(P_1\right)$$

$$\text{System} = \begin{pmatrix} 1 & -1 \\ -1 & 1 \end{pmatrix} \begin{pmatrix} 1 & 0 \\ 0 & \exp(i\varepsilon) \end{pmatrix} \begin{pmatrix} t(r) & 0 \\ 0 & t(r+\Delta r) \end{pmatrix} \begin{pmatrix} 1 & 1 \\ 1 & 1 \end{pmatrix} \begin{pmatrix} U_0 \\ U_0 \end{pmatrix} \tag{16}$$

Here, a Nomarski prism (a modified Wollaston prism, NP) splits the fields (on the sample plane) into two polarizations, that traverse the sample (t) at slightly offset positions (Δr). An output polarizer, external to the microscope and at -45° (P_2), analyzes the light, allowing the two orthogonal polarizations to interfere. The phase shift between these beams is controlled by an SLM, acting as a variable retarder between the two polarizations (ε is cycled), which enables the interferometric recovery of the phase difference ($\Delta\phi$) along the sample (Figure 6, field spatial shift). Thus, at the camera, the two polarizations become:

$$
\begin{aligned}
U_x &= U_y \exp(i\pi) = (t_1 - \exp(i\varepsilon)t_2)U_0 \\
I &= |U_x|^2 + |U_y|^2 = |t_1|^2 + |t_2|^2 + |t_1||t_2|\cos(\phi_2 - \phi_1 + \varepsilon) \\
I &= I_0(1 + \gamma\cos(\Delta\phi_r + \varepsilon))
\end{aligned}
\tag{17}
$$

where ϕ_1 and ϕ_2 represent the change in phase accumulated from the sample at t_1 and t_2, respectively.

Here the phase shift due to the object can be received from four frames as:

$$
\Delta\phi_r = \tan^{-1}\left[\frac{I_{-\pi/2} - I_{\pi/2}}{I_0 - I_\pi}\right]
\tag{18}
$$

Although the raw visibility on the detector is smaller compared to phase contrast, there are notable advantages owing to the close coupling of the contributing fields. As the intensity in the two fields is necessarily balanced, the scheme achieves optimal visibility in turbid media. Further, when compared with SLIM or DPM, the interference is formed between two points within the diffraction spot rather than between a self-generated background reference, avoiding halo artifacts [65]. Further, the phase-shifting element can be placed anywhere in the optical path and the whole configuration can be realized in backscattering (reflection geometry) enabling surface material science applications (*i.e.* imaging silicon wafers [66, 67], surface roughness inspection [68]).

Note that in GLIM, we measure $\Delta\phi_r \simeq \nabla_r\phi$, *i.e.*, the gradient of the phase and not the phase itself. Thus, for quantitative phase information, we need to integrate the GLIM data.

In our implementation, it is possible to switch between SLIM and GLIM by moving a polarizer and switching the microscope to DIC illumination.
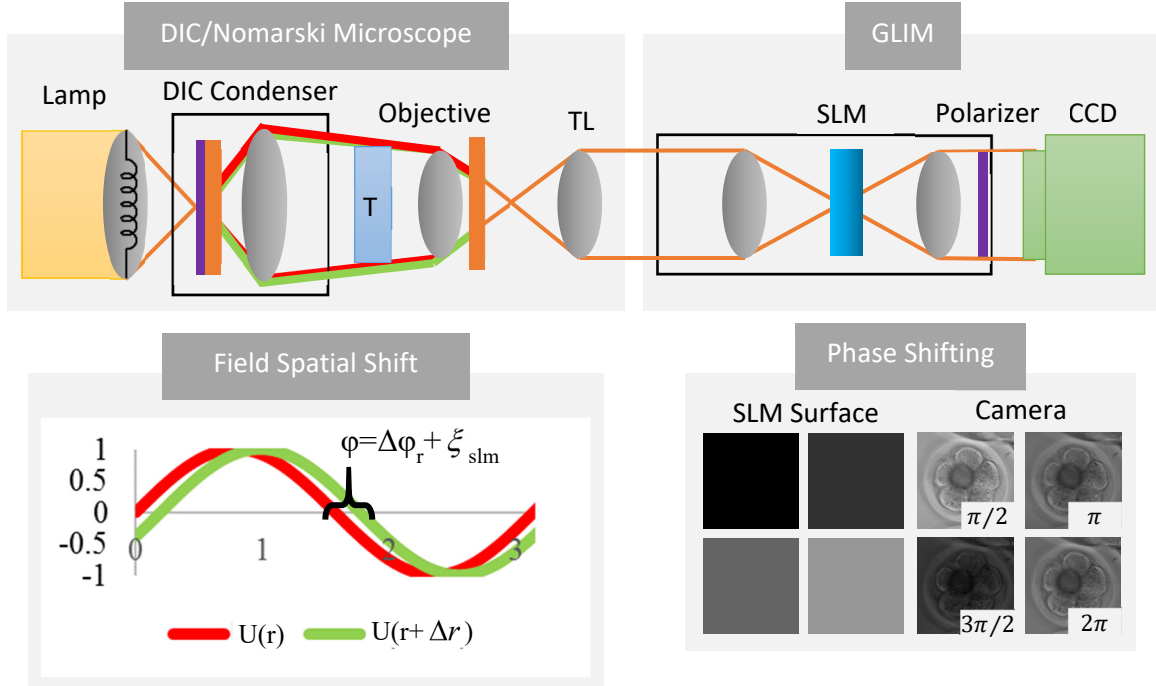
Figure 6: GLIM geometry. The Nomarski prism in a DIC microscope (orange component) splits the incoming light into two polarizations (green, red), that traverse the specimen at laterally offset positions (Δr). The output Nomarski prism recombines these two fields spatially, and the output polarizer adjacent to the camera allows them to add coherently at the detector. The relative offset between these two fields is modulated by the SLM (ϵ_{slm}), with four such images used to recover the phase difference across the specimen.

2.2.4 Summary

Table 1: Comparison of Our QPI Add-on Systems

	Speed	Sensitivity	Strong Scattering
DPM	+		
SLIM		+	
GLIM			+

In summary (Table 1), DPM provides high-speed imaging at the expense of the sensor spatial bandwidth and sensitivity. By phase shifting the phase contrast field, SLIM has exceptionally high sensitivity although strongly scattering samples introduce imaging artifacts when the reference field is significantly distorted by the sample. To remedy this problem, GLIM maintains the geometric stability of common-path systems without the artifacts typical of "self-referenced" interferometers, making it well suited for imaging turbid specimen.

CHAPTER 3: FRAMEWORK FOR MULTISCALE IMAGING

This chapter outlines the design of an automated platform for phase imaging. Such a system is well motivated as previous approaches were slow and experimental operation required an engineering background. We developed a dedicated software to meet both of these challenges.

The software overlaps computation with hardware events, such as SLM modulation or camera transfer time. The interface wraps an OpenGL 4 context inside Digia's Qt5 framework. To achieve real-time performance, three decoupled threads operate in pipeline fashion. The first thread is responsible for triggering the acquisition of new images and controlling the spatial light modulator (SLM). A second thread receives and transfers new images to the GPU, with a third thread rendering the phase images (Figure 7). The rendering procedure is quick compared to the acquisition time, with the full 4-megapixel frame computed in less than 8 ms for SLIM/GLIM and 12 ms for DPM on a GeForce 780 card.

This "producer-consumer" model is necessary as scientific cameras, have precise shutter-open triggers but the availability of acquired data (at the millisecond scale) depends on computational load along with the specific hardware being used. As an example, assume a camera can be triggered every 10 ms, but data arrives at 12 ms ± 2 ms. Without this scheme, realized throughput would be 14 ms rather than 10 ms, and the camera aperture jitter would perturb time critical experiments such as the dynamic light scattering studies. With the Windows multimedia timer service, along with disabling high-latency hardware devices, aperture jitter can be reduced to under a millisecond.

To avoid redundant memory copies, a large buffer is acquired at program initialization, and pointers to this buffers, rather than memory copies, are passed between threads. Further, these pointers are used to detect acquisition failure by verifying the order and arrival of triggered frames from the camera's API. When an error occurs, the acquisition event is repeated, although some categories of errors require

the camera to be reset in software. In these cases, the necessary synchronization is handled by a recordkeeping structure, where frames are pooled into three categories: "free", "inside camera", and "inside IO". In the event of an error, a lock is held until the necessary corrections are made, resetting the camera or waiting for more files to be written to the disk, implicitly pausing the acquisition threads.

To facilitate scanning microscope slides (see Chapter 5) and other forms of programmed automation, the interface generates acquisition lists outlining the state of the microscope for each event (Figure 8). This list is then processed, with one thread dedicated to triggering the camera, shifting the
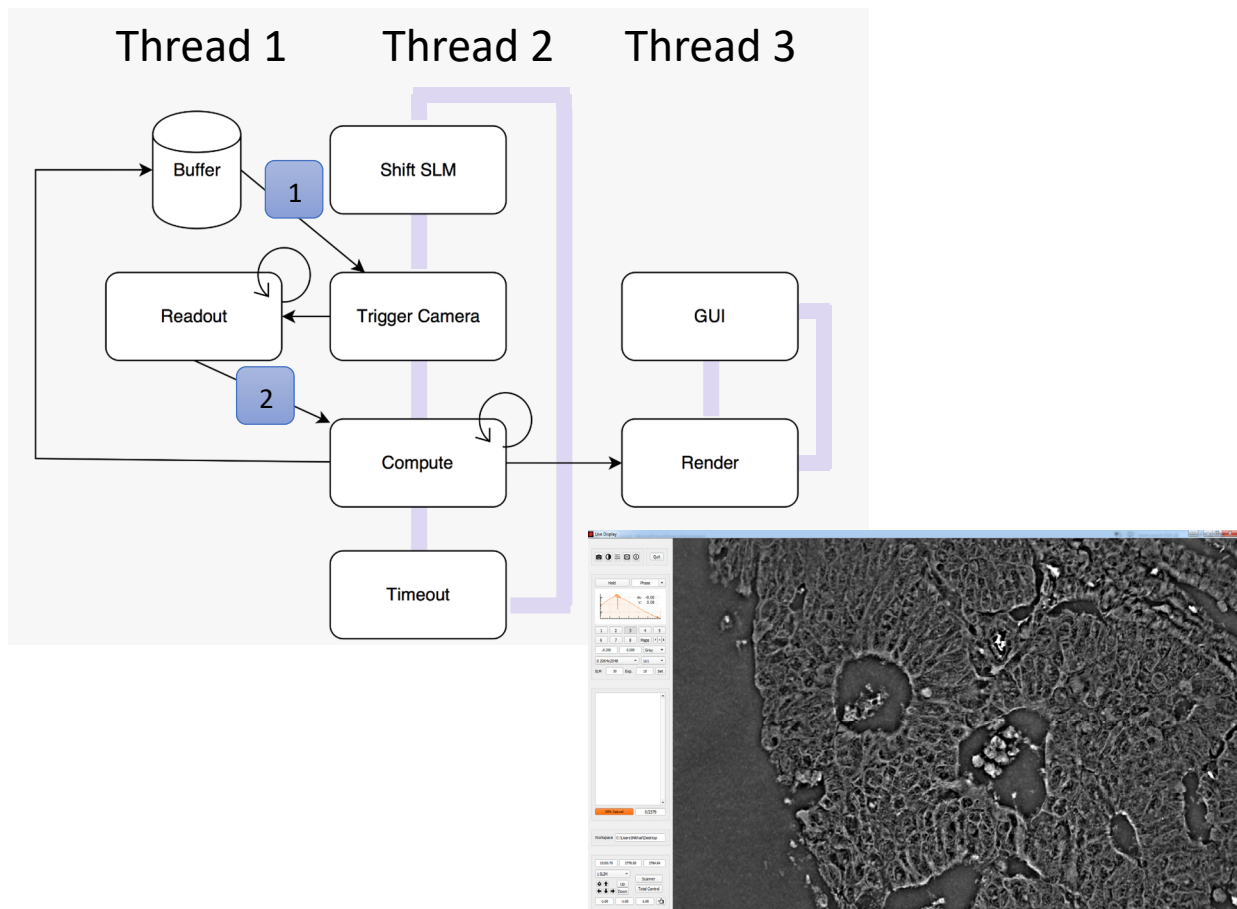
Figure 7: Live rendering. The live interface performs the phase retrieval process in real-time with the imaging presented as a microscope channel similar in operation to existing fluoresce or transmitted modalities. To account for any mismatch between consumer and producer threads, the "triggering" process (Thread #2) releases a single frame while the readout process is capable of receiving multiple frames (Thread #1). In GLIM and DPM, further filtering steps are performed, such as Fourier filtering to remove background artifacts.

SLM, and moving the microscope. A second thread is responsible for receiving the images, computing autofocus parameters, and recordkeeping to redo frames in the case of acquisition failure. Finally, a third thread is responsible for writing files to the disk.

The system is able to sustain approximately 15 four-frame reconstructions (SLIM or GLIM) per second below which image quality and phase accuracy degrade, along with a significant increase in aperture jitter and data transfer error. Single-shot DPM images are rendered at 60 hz as limited by conventional computer monitors. For phase-shifting modalities, the principle limitation is SLM stability, as exposure times can be reduced by simply increasing the intensity of the illumination, while the best reported SLM stability times (for green light) are around 4 ms [69].
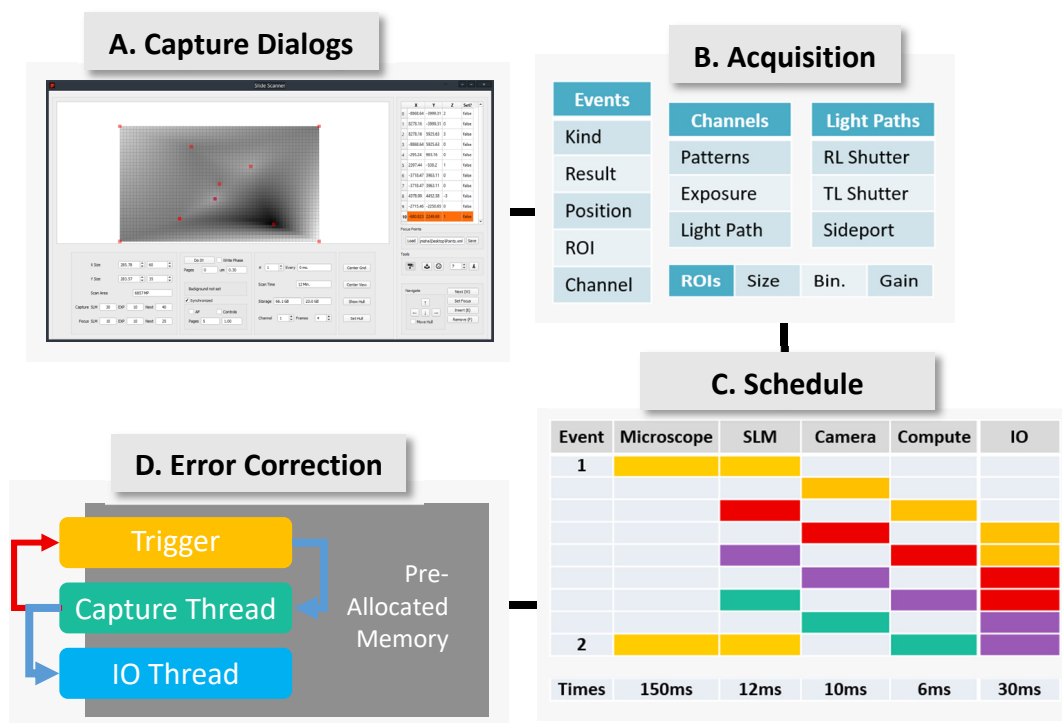
Figure 8: Software architecture. The capture interface (A) generates a list of events (B) that is acquired according to a pipelined schedule (C). The capturing framework tracks and repeats failed acquisition events (D).

CHAPTER 4: HIGH SENSITIVITY APPLICATIONS

4.1 Microtubule Dynamics

In addition to usability issues, another factor limiting the widespread adoption of quantitative imaging is the perceived lack of visual quality in the phase map when compared to the raw data used to recover the phase information [70]. Here we provide a counterexample, by demonstrating that the phase map in SLIM provides a holistic improvement over phase contrast for imaging small, sub-diffraction structures [38].

To this end we choose to study microtubules, which are cytoskeletal elements with incompletely understood dynamic properties [61, 71-78]. Beside their structural role in eukaryotic cells, microtubules provide pathways for motor-driven cellular cargo [79, 80]. Due to their ubiquitous role in intracellular transport, motility, and proliferation, microtubule malfunction has been associated with various diseases, from cancer [81] to Alzheimer's disease [82].

Despite decades of research, studying single microtubules dynamics is challenging due to their tiny dimensions; consisting of a hallow tube with a 24 nm outer diameter and 12 nm inner diameter. Our technique addresses the key difficulties with competing methods such as darkfield microscopy and video-enhanced differential interference contrast (VE-DIC) [83-85]. Unlike darkfield, our system benefits from enhanced phase sensitivity enabling us to acquire high-contrast images of unlabeled microtubules. Unlike DIC, our system avoids the directional shading that makes parallel microtubules difficult to resolve. As shown in Figure 9, when compared to phase contrast, our interferometric reconstruction removes the non-trivial background due to out-of-focus illumination. In simple terms, incoherent contributions do not respond to phase shifting and are subtracted out during phase retrieval. To further enhance the image, we apply a five-tap median filter and a spatial bandpass filter [86]. Owing to the simplicity of the scheme, with the median operation implemented as a per-pixel sorting network [87], the computation is fully

masked by the acquisition process. This is to say, the SLM modulation and camera integration times are longer than the phase retrieval and digital image enhancement.

Compared to fluorescence imaging, the object's scattering potential does not photobleach (Figure 10), which enables virtually indefinite observation over larger fields of view then competing methods [88]. To demonstrate utility of our technique, we performed a conventional gliding assay of motor protein motility (Figure 11) [89], and extended it to emphasize our new found ability to perform long-term imaging. In our new assay, we observe microtubules for a period of time over which the "fuel", *i.e.*, ATP (Adenosine triphosphate) is exhausted and recover the "dispersion relation" governing the advection velocities. Thus, using dynamic light scattering avoids tedious manual tracking (Figure 12) [90]. Here the manual method agreed well with the automatic analysis. As the ATP is exhausted, the spread in observed gliding velocity tends toward zero, indicating that the gliding stops.
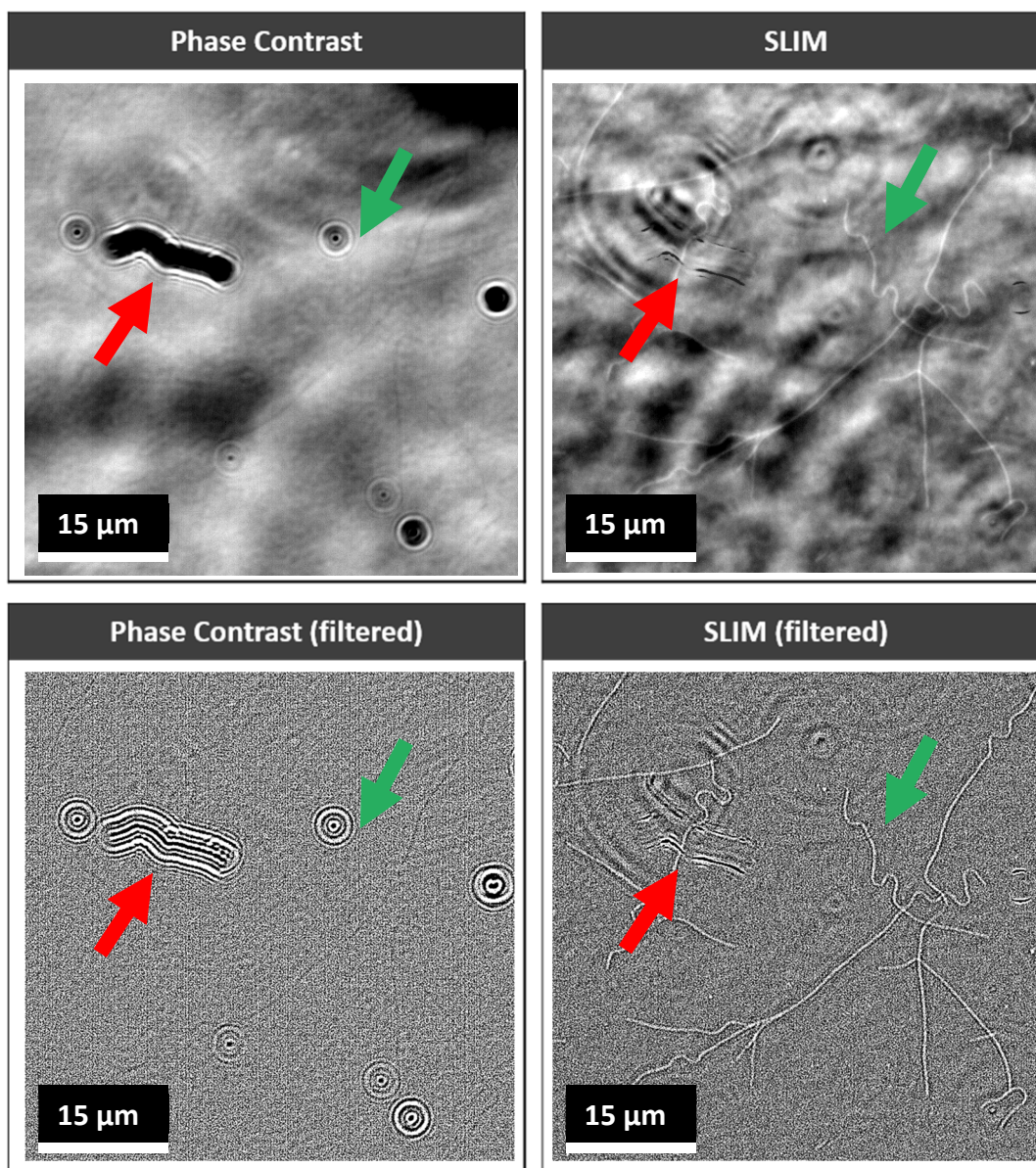
Figure 9: SLIM improves phase contrast. Left panel shows a select portion of the phase contrast frame use in the SLIM interferometric reconstruction process. By removing light outside of the coherence gate, the SLIM system performs implicit background subtraction, taking the phase contrast frames into the "canonical contrast basis" (a phase map). The phase map is free of amplitude defects (red arrow, scratch on the objective), and provides a significantly flatter field of view (green arrow). Features larger than 3 pixels were removed from the bottom row, using a Fourier bandpass technique, highlighting that the contrast improvement comes from our hardware system rather than the outcome of digital image processing. This images were acquired under 63x/1.4 illumination.
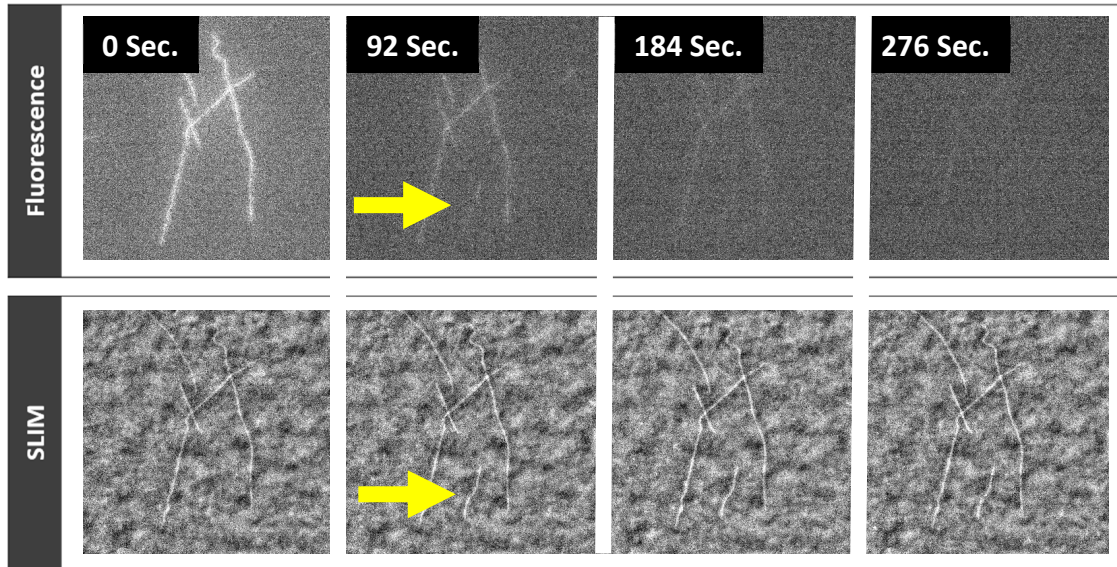
Figure 10: SLIM enables continuous observation without photobleaching. Note that a descending microtubule is not visible due to photobleaching. The sequence was acquired under 63x/1.4, and to better simulate typical fluorescence imaging conditions the shutter was closed between frames. For easier visualization, the SLIM sequence was filtered with a highpass filter along with a rolling five-tap median. This processing runs in real-time on our acquisition system.
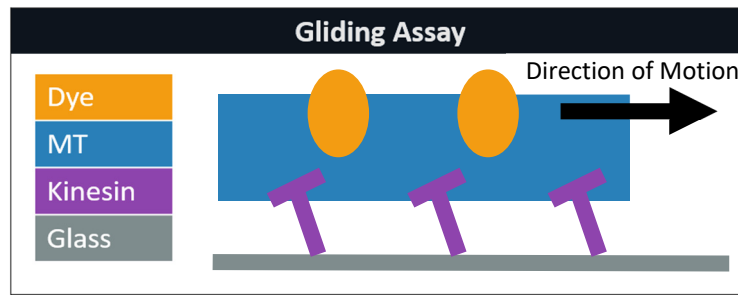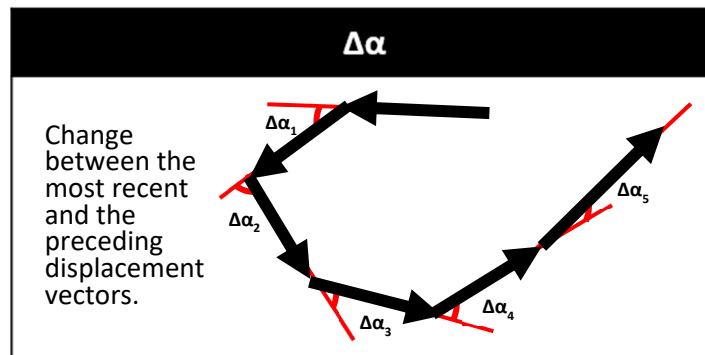
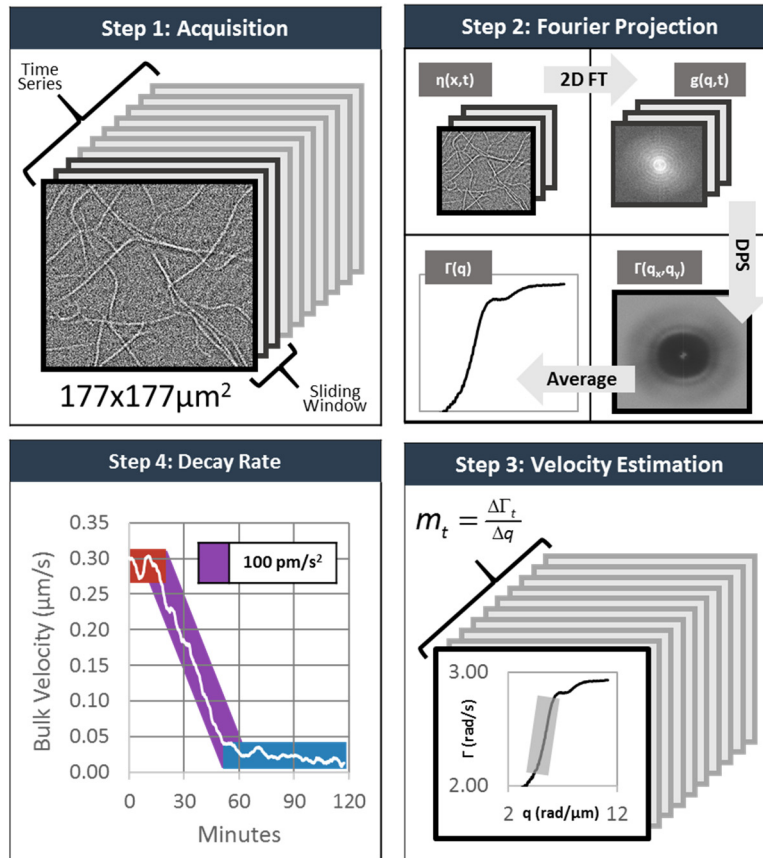**Figure 11: A gliding assay with SLIM.** In a typical gliding assay (top) microtubules are pushed by surface attached motor proteins. The gliding velocity of the microtubules provides a measure of the protein's motility. Example of the assay performed with SLIM under 63x/1.4 [38].

Figure 12: Comparably longer imaging enables the investigation of motility decay constants. Microtubule gliding velocities were calculated in bulk using dispersion-relation spectroscopy on a rolling basis over ~15,000 frames taken 0.475 seconds apart (step 1). For each frame, 512 (~245 seconds) time slices were used to obtain the spatial-temporal autocorrelation function (g), after further refinement a radial average is used to obtain the spectral decay Γ (right subplot). Subsequently (step 3), a line is used to obtain a velocity coefficient for each time point. When plotted over time, after twenty minute since the start of imaging, the velocities of the microtubules begin to decay, with virtually no motion present past the sixty-minute mark.

4.2 Cell Population Dynamics

While typical assays of cell growth seek to investigate unifying trends, such as average growth rates in response to stimuli [38, 91], it is becoming increasingly evident that what appear to be homogenous populations in reality can have individuals that express very different phenotypes [91]. To facilitate quantifying the degree of cell-to-cell variation, we proposed a technique that exploits SLIM's accuracy to highlight disparities in the growth behavior of cells, assigning a "degree of influence" score to each

cellular cluster [92]. In contrast to other methods that assay cell growth and proliferation [93], the score can be mapped back to the original image hinting at the underlying cause of the disparity.

The technique proceeds by segmenting the cells into clusters, using an *ad-hoc* approach where edge detection is followed by morphological dilation. Crucially, these filters are applied along the temporal and spatial dimensions (2D+T) which facilitates easy removal of false positives, in particular moving debris (Figure 13). Next, the algorithm assigns a growth rate coefficient to each lineage by fitting an exponential to the measured phase [94, 95] (Figure 14). Lastly an influence score is calculated by considering the relationship between the distance and growth rates for neighboring clusters (Figure 15). For example, if there is a uniform growth rate drop near a cell that is understood to have a high influence on its surroundings.
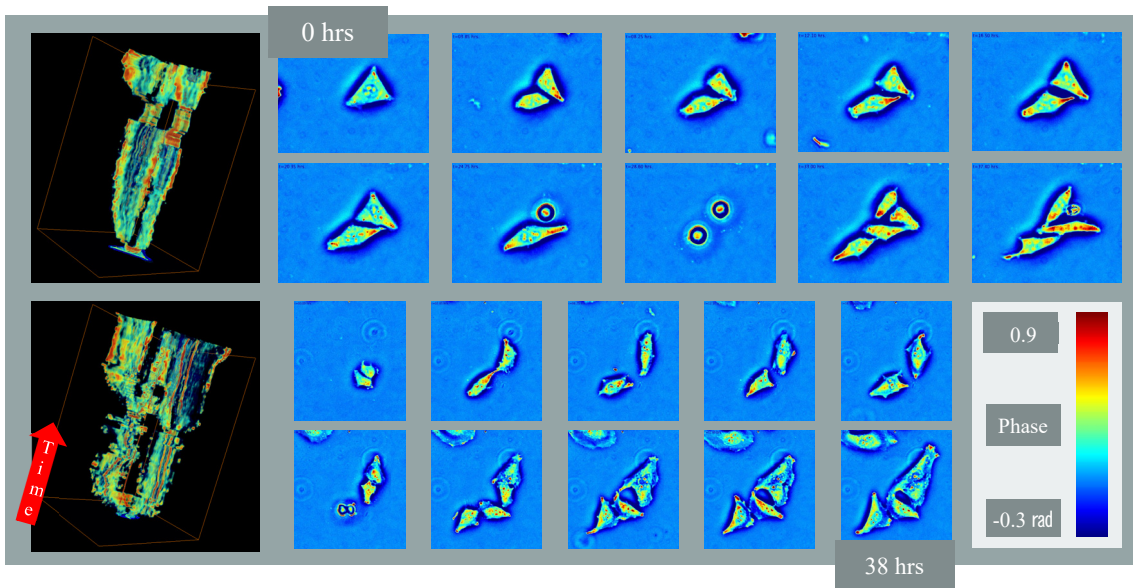
Figure 13: Step 1, segmentation. After application of a 3D edge detector followed by a blurring kernel, it is possible to extract cell growth lineages, two examples of which are shown. The images were acquired with a 20x/0.3 objective.
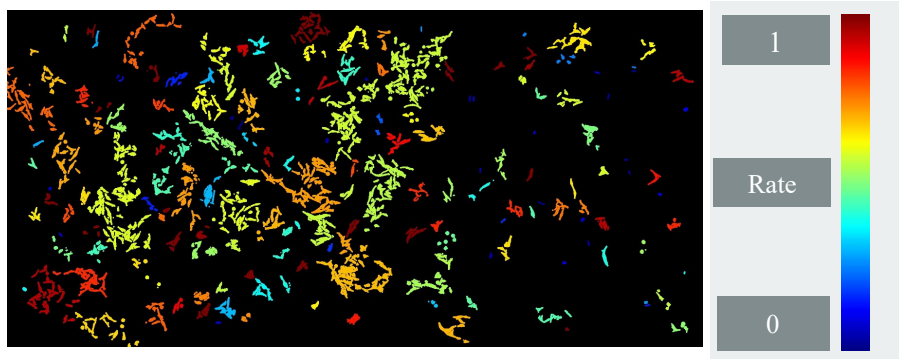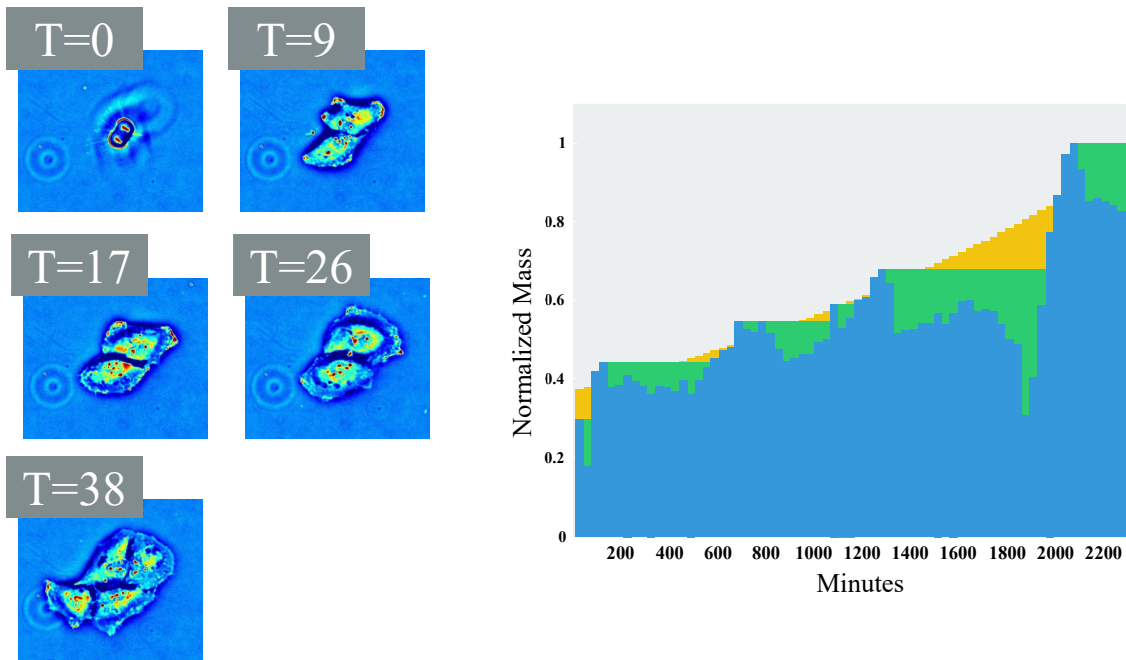
Figure 14: Step 2, growth rate calculation. The measured mass (teal) is smoothed after application of a "no-negative" growth prior (green), which is fit to an exponential (orange). The normalized growth rate of this exponential is used to label the cluster (bottom).
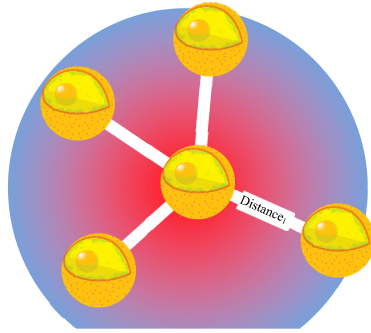
$$R = \frac{\mathrm{cov}(\mathrm{Distance}, \mathrm{Growth})}{\sqrt{\mathrm{cov}(G,G)}\sqrt{\mathrm{cov}(D,D)}}$$
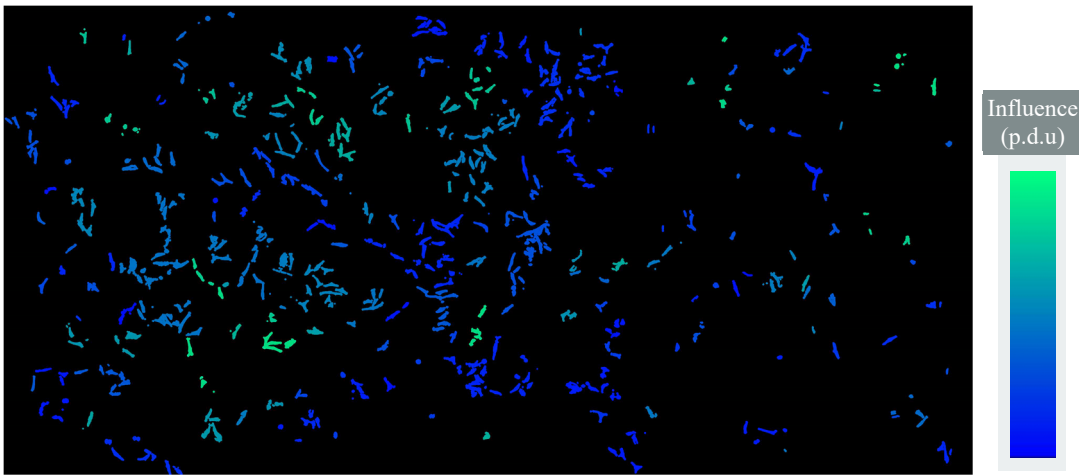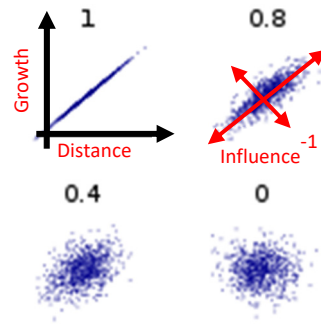
Figure 15: Step 3, connectivity analysis. The intuition underlying the method (left panel) along with typical distributions for Pearson's R (right panel) [96] (underlay from [90]). In the bottom figure the method was applied to approximately 150 clusters with approximately 14 neighbors in each cluster. The window size is adjusted until no qualitative change is observed in the image. At a glance, cells on the edges drive the growth of their neighbors.

CHAPTER 5: TOMOGRAPHY

5.1 Tomography Using SLIM

Owing to their small size, cellular structures are typically studied under high resolution [97, 98]. The spread of information along the depth gives rise to a smear that makes visualization and analysis non-trivial. Although there are numerous proposed methods to measure and remove this blur, principally by deconvolution, due to limited momentum space coverage ("missing cone" [99, 100]) typical success stories in full-field optical microscopy have been limited to intrinsic contrast agents [101-103]. While there exist hardware solutions such as rotating the illumination or sample (among others [104, 105]), these methods are invariably cumbersome for studying populations of living cells. Instead, a typical experimentalist will simply switch to a point scanning or electron microscopy [106, 107], which, owing to the fixation procedure or slow scanning rates (or both), cannot be used with living cells.

Instead, we aim for a physically motivated technique to highlight cellular compartments and traffic. After assuming the gradients of the electric and magnetic permittivity are comparably small, Maxwell's equations, for an open region, can be reduced to the well-known inhomogenous Helmholtz equation [108]. With the phase map ($e^{i\phi_r}$) recorded by our QPI system, the equation is easily solved. In this implementation, the Laplacian is performed in the spectral domain [109].

$$\nabla^2 U + k^2 n^2 \left(\overline{r} \right) U = 0$$
$$k^2 n^2 = -\nabla^2 e^{i\phi_r} \big/ e^{i\phi_r}$$

(19)

The resulting image can be rendered to extract the isosurfaces (hyperplanes) required to calculate parameters such as density (Figure 16). Due to the intrinsic self-normalization of the phase information ($e^{i\phi_r}$) these thresholds are invariant for the duration of the image sequence, and do not show appreciable variation between individual cells.

Figure 16 shows a typical use, where time lapse tomograms are acquired every minute, for an extended

duration of time. The cellular cargo is visible appears as balls inside the extension. The flux of mass

through cellular extensions is the mechanism of neuron growth and recovery [110-112].
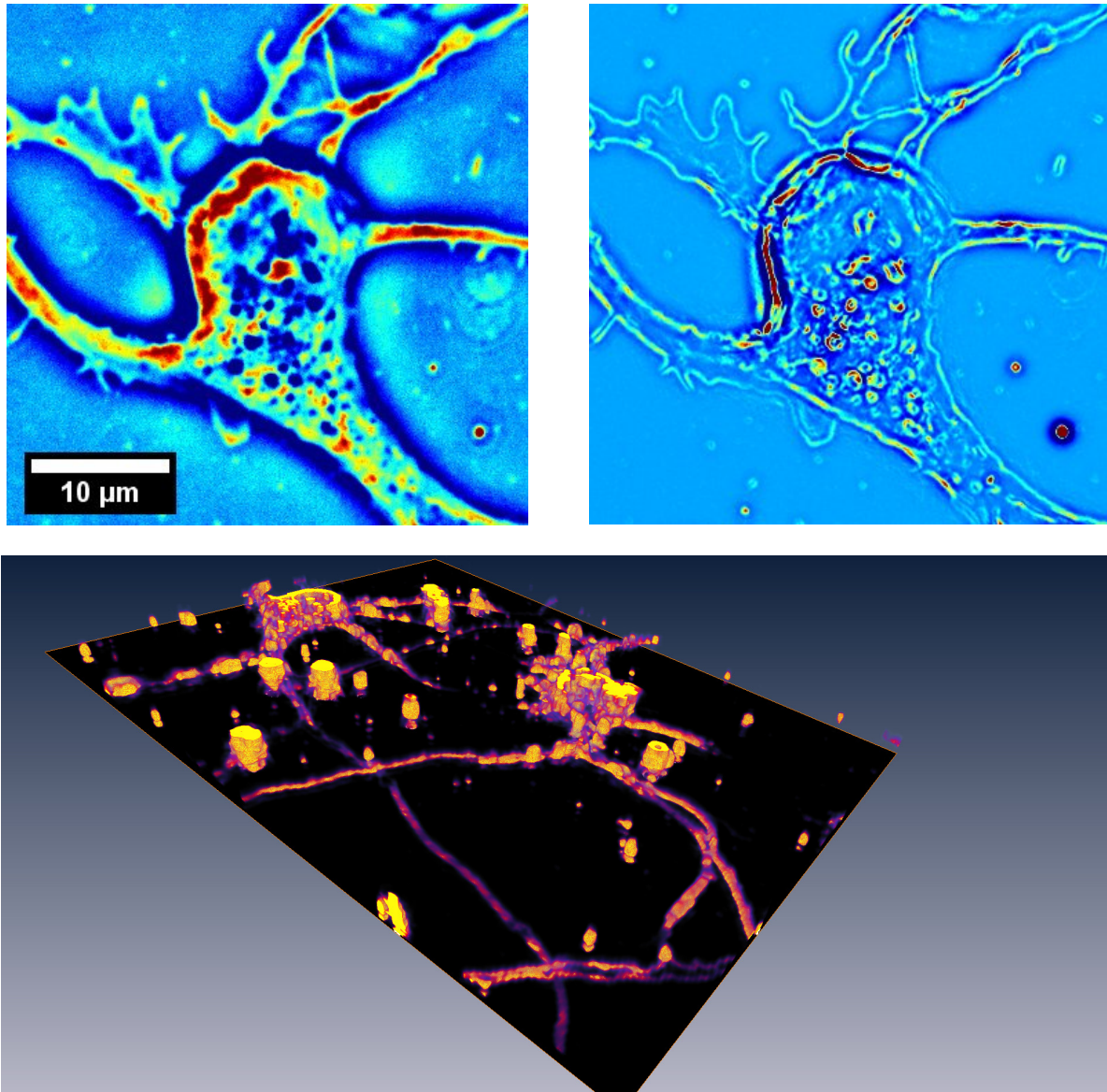
Figure 16: 3D rendering of a neuron cluster. Top-left panel shows a zoomed portion of a SLIM image acquired with a 63x/1.4. In the top-right panel, the image has been filtered with the proposed scheme. While the SLIM image (left) is purely two-dimensional, the filtered result (right) uses data acquired at different planes. The bottom panel shows the resulting rendering. Both figures are displayed in arbitrary units as the rendering procedure is invariant to constant scaling.

5.2 Tomography Using GLIM

The chief advantage of differential interference contrast compared to phase contrast comes from the close coupling between the contrast forming wavefronts. As the orthogonal polarizations in DIC traverse nearly the same path, the power is matched and the halo artifact typical of phase contrast is non-existent. Furthermore, compared to a typical phase contrast microscope, the sectioning capabilities in DIC are tunable by opening and closing the condenser. Note that attempting to expand the ring illumination in PC would not only require specialized hardware, but also result in a drastic reduction in contrast (Figure 17). Lastly, the illumination in GLIM, necessarily, has a broader coverage of spatial frequencies due to the larger surface area of the illuminating pupil, leading to improved sectioning compared to phase contrast (SLIM) [113] (Figure 17).

Although the illumination contains a broader coverage of frequencies, the contrast in DIC is not directly related to the refractive index of the object, introducing immediate artifacts that must be compensated. Specifically, as the interferometric image is related to the derivative of the object's phase information, it is desirable to integrate the image along the direction of the shear (Figure 18). As the shear between the image forming polarizations is unidirectional, the sample contrast orthogonal to this shear direction is lost. This results in a "wedge" shaped contrast transfer function (Figure 18, red areas have object information).

Figure 19 shows an example of a structure, a *C. elegans* nematode, that would be difficult to observe with SLIM.
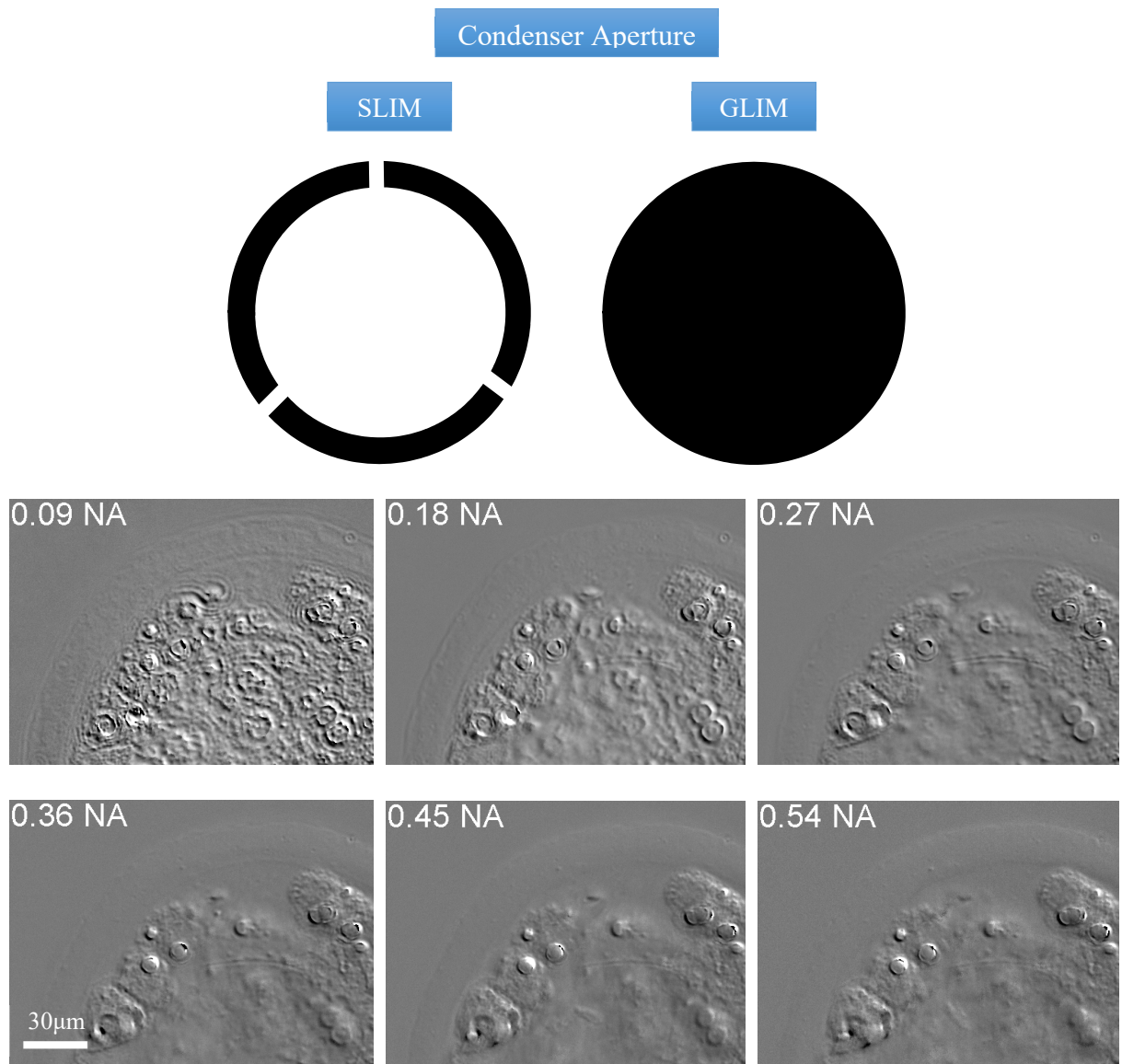
Figure 17: DIC illumination is well suited for tomography. Top panel highlights the surface area difference between DIC and PC illuminating apertures (shared). The bottom panel shows that the sectioning can be adjusted by changing the numerical aperture of the condenser. Mouse embryo imaged with 40x/0.95, at various condenser NA values, as indicated.

GLIM (raw)

GLIM (integrated)
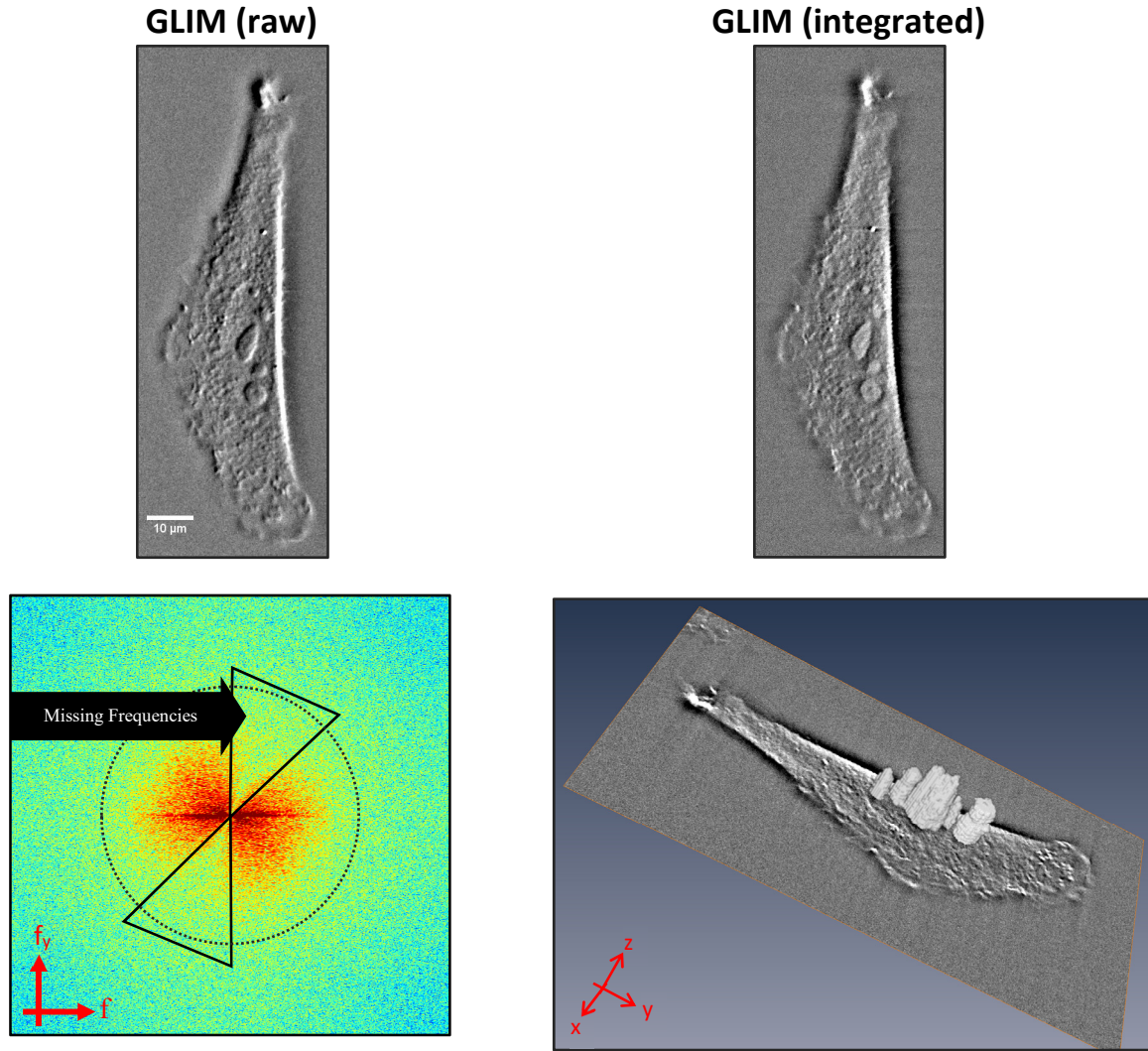
Figure 18: Removing DIC artifacts. Top-left panel shows the GLIM image and the right panel is the result of a Hilbert transform demodulation technique which aims to removing the right-to-left shading typical of DIC images [114]. Bottom-left panel shows the spectrum of the input image with missing frequencies orthogonal to shear direction. Dashed ring approximates the diffraction limit. Bottom-right panel shows a HeLa cell (40x/0.95) rendered to highlight nucleoli (gray volumes) which can be used to calculate parameters such as surface area or density.
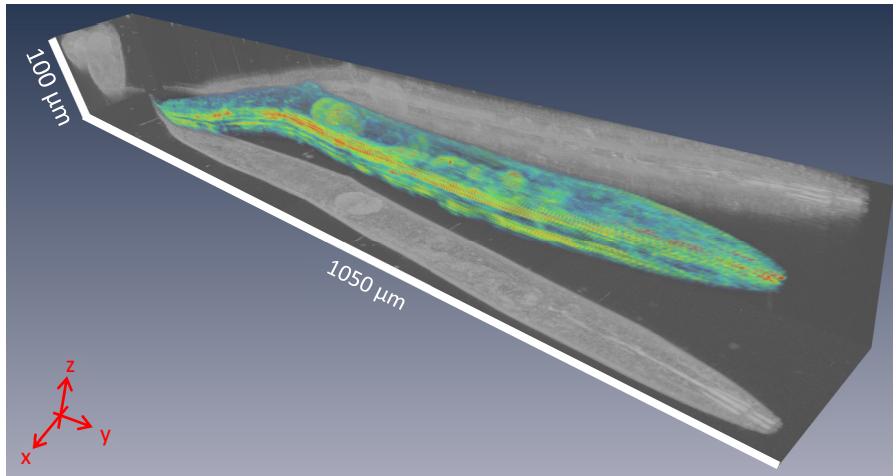
Figure 19: Imaging large structures with GLIM. Rendering of a whole nematode showing how GLIM can be applied to larger structures, the waving/standing behavior appears to be a form of nictation, where the nematode searches for a new environment [113].

CHAPTER 6: QPI TISSUE SCANNER

6.1 Interface

This chapter contains a description of a design for a slide-scanning module and the associated computational post-processing tools required to assemble the acquired data [43].

The scan is performed offset from a user-defined plane (Figure 20), which is generated by querying a Delaunay triangulation [115]. At each tile, the estimated focus plane can be further refined by automatically scanning through the depth to maximize the "focus function" (Figure 21). Although, iterative techniques such as Golden-Section-Search [115] showed promise, they were found to be significantly slower as the mechanized focus needed to traversal a larger distance and, critically, it was impossible to overlap acquisition with computation — requiring the whole frame to be acquired, and
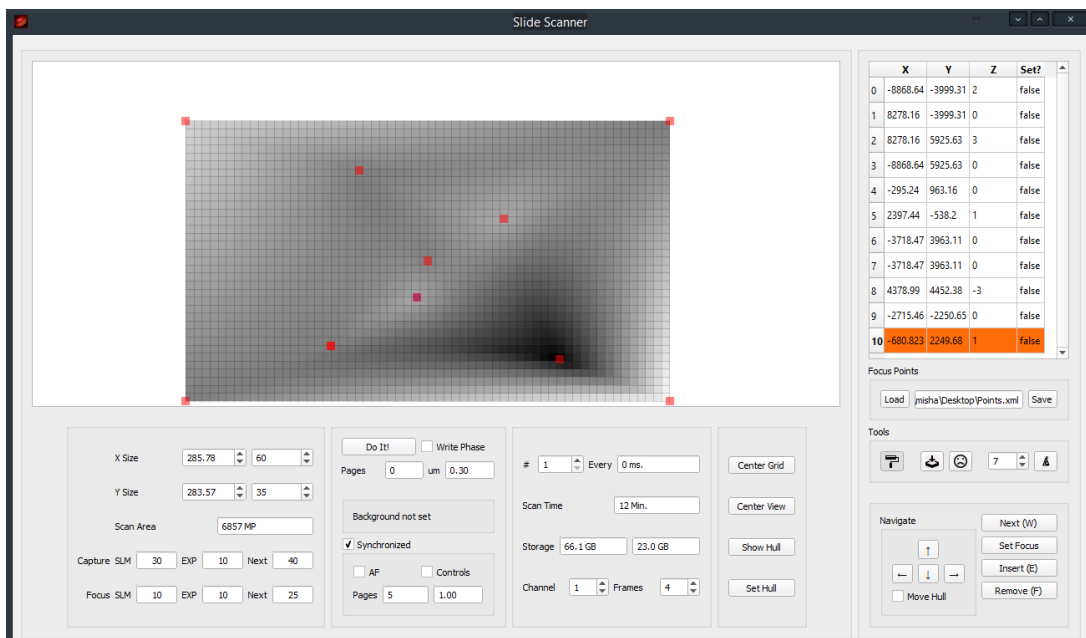
Figure 20: Scanner Interface. The "plane of best focus" is drawn as a rectangle with shading indicating height variation due to manually selected focus points (red squares). The autofocusing system proceeds from this initial guess by performing a depth scan at each tile position.

processed before subsequent acquisition. In addition to effectively doubling the time needed per z-slice, using a convex optimization technique is, fundamentally, unreliable because noise renders the focus curve non-monotonic. Unlike a linear search, a misstep at the first bifurcation is irreversible and leads to a drastic deviation from the optimal result. Thus, our implementation uses a linear sampling and performs approximately five depth scans per seconds.

6.2 Autofocus

After sampling the focus function, the algorithm performs a parabolic interpolation to choose the final image (Figure 21, black circle). Here we used a universally applicable interpolation scheme and did not pursue the direction further. The focus metric is based on the intuition that adjusting the focus knob brings the image in and out of view. When the lines that constitute the image "come together" the sample is understood to be "in-focus". Therefore, we choose to maximize the variance of the 2D wavelet decomposition, specifically Haar wavelets which are a basis of edges — well suited to describe transient discontinuities [116, 117].

The robustness of this metric can be assessed by its performance on cases where the plane of best focus is ambiguous. Such a case frequently occurs in live cell imaging, where there is a tendency for individual cells to round up away (bulge) from the glass during division events. The membrane circumscribing the cells appears as a sharp discontinuity and contributes disproportionately to the overall image variance. This leads to a counterintuitive best focus. In the extreme example shown in Figure 21, the membrane is in focus while the surround cells are not. Similar defects can be found in clinical tissues, due to residual paraffin. By using a heuristic that chooses the "most in-focus volume" with the "highest contrast", the "fusion" scheme selects the expected result where most of the cells are in focus. Owing to the precision of the stage along, with the numerical repeatability of interferometric measurements, relatively large steps (2um) can be used to localize the plane of best focus.
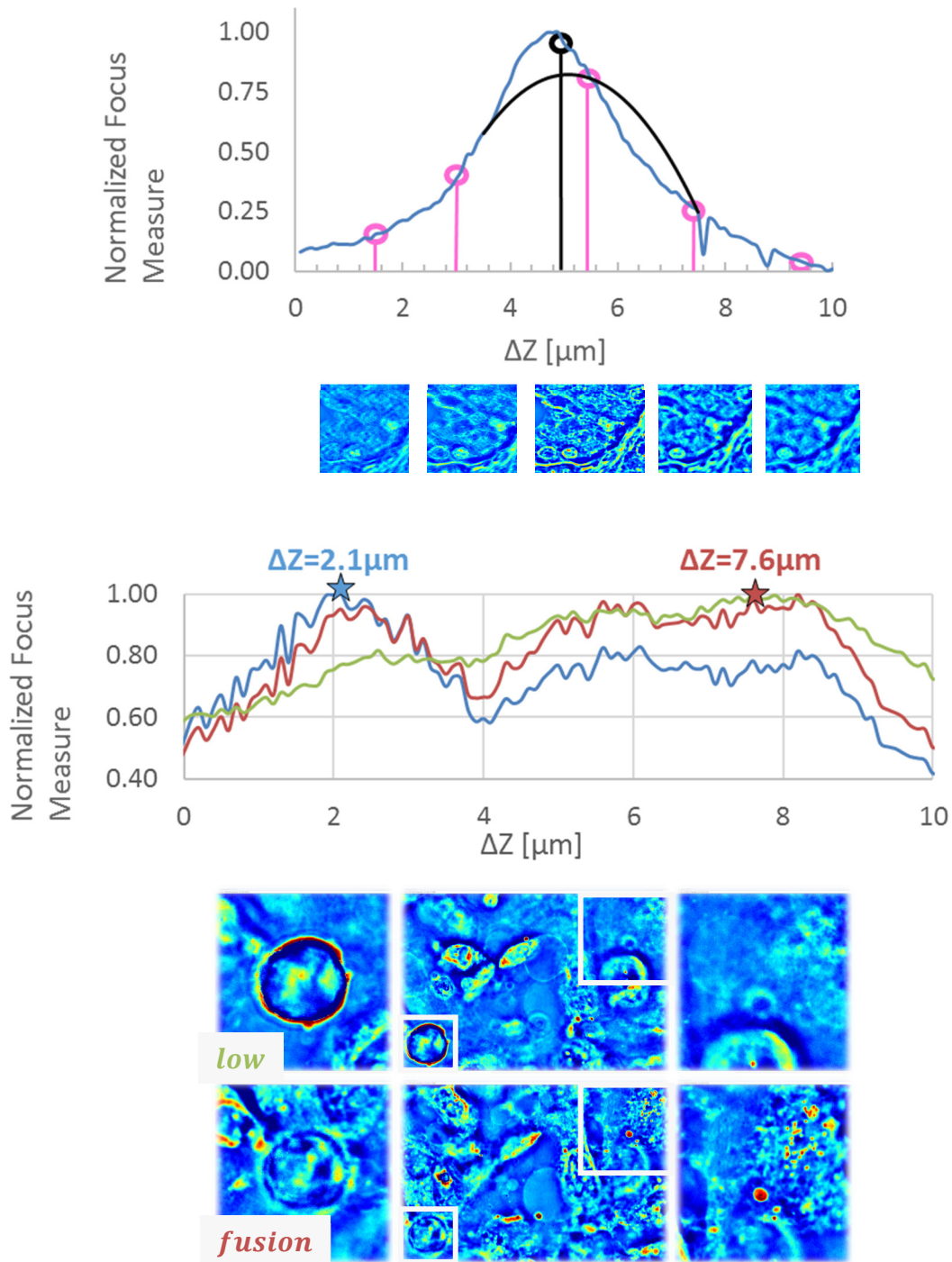
Figure 21: Depth scanning autofocus. Several images acquired at different planes are used to estimate the optimum of the focus function with the final acquisition (top, black) performed at the optimal location determined by a Gaussian interpolation function. The focus metric was calculated by computing the variance of Haar wavelet detail images (bottom panel).

6.3 Image Assembly

Mosaic tiles are acquired by translating a motorized XY stage, with the understanding that there will be a rigid misalignment (x,y drift) in the assembled image. To address this problem, we developed a program that registers the tiles by optimizing the spacing between overlapping regions [118].

To avoid memory limitations, the software performs two passes on the data, with the first pass finding the optimal overlap and the second pass generating tiles for archival storage. The alignment procedure is pipelined in order to mask computation with disk access, with one thread responsible for loading data into a large buffer and a second thread performs the computational portion of the phase correlation procedure. Further, when possible, image reads are stored in a cache so that subsequent reads do not require disk access. When system RAM is exceeded, the oldest image is removed from the cache. The required real-to-complex discrete Fourier transforms are performed on the GPU, with the computational portion occupying less time than disk access. An additional performance increase comes from ordering the phase correlation pairs so as to avoid redundant computation, and caching the results of old computation. In most cases this scheme is able to avoid one of two of the Fourier transforms in the phase correlation algorithm.

Disagreement between the true position of a tile is resolved by a least-squares fit, producing a globally optimal tile configuration with minimal alignment error. On the second pass, mosaic tiles are arranged according to this optimal configuration, and the resulting images are generated for web viewing (JPEGs) or archival storage (TIFFs). While overlap between mosaic tiles could be combined to achieve a more aesthetically pleasing seam, to avoid affecting the quantitative image statistics (in particular, the variance [119, 120]), overlapping regions contain data from only a single mosaic tile. Finally, background correction is applied by selecting a small percentage of the data whose phase values are near zero and presumed to be empty space, and subtracting the background from each constituent frame. Following the initial tile generation, successive levels are merged to create the mipmaps ("image pyramids") which facilitates rapid zooming and panning.

For rapid development, the code was written in Python with the GPU portions using PyCUDA. The rate limiting steps is disk access and writing, which in principle can be ameliorated with more expensive hardware. Here, we used CATMAID and Zoomify, with the principle advantage of CATMAID being easy annotation [32] and Zoomify operates without a dedicated server. Figure 22 shows a typical slide.
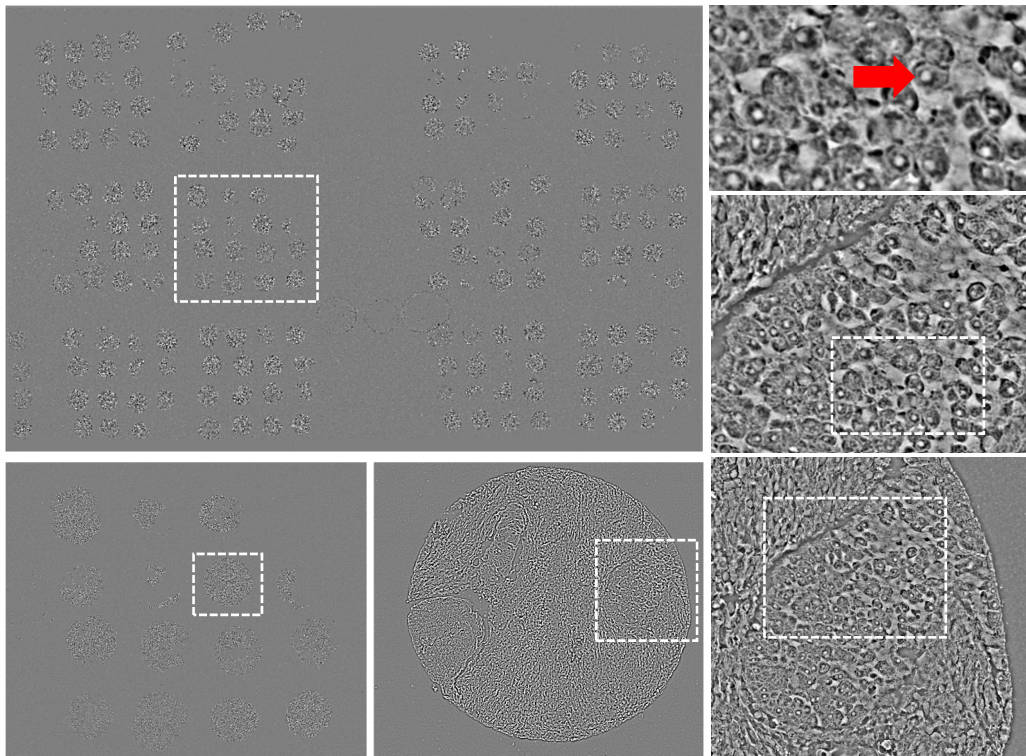
Figure 22: Typical tissue core microarray slide [43]. The automated image processing system reduces 200 GB of interferometric data into a pyramidal image format that can be accessed remotely. Owing to the submicron resolution in SLIM, details such as individual nucleoli are clearly visible (red arrow). This sample was digitized in approximately 45 minutes, with another 15 minutes to assemble the SLIM tiles.

CHAPTER 7: OUTLOOK

The previous chapters presented the motivation, operation, and new applications enabled by our new high-throughput imaging systems. This chapter contains a discussion of some of the outstanding challenges for future instruments along with proposed solutions. The challenges can be roughly grouped in terms of cost of ownership, imaging speed, and object reconstruction from phase information.

In terms of cost, phase shifting QPI systems can be expensive owing to the use of SLMs. Although SLMs simplify alignment, the pattern written on the detector is usually a simple ring, dot, or uniform value which can be replaced by a modulating piston. Furthermore, if more control is required, a transmission SLM, such as the one found in a consumer grade ("conference room") projector, can be used [43]. In the case of GLIM, where the modulation takes the form of a uniform gray value (piston), an electronically controlled variable retarder can act as a single pixel SLM, avoiding moving parts while simultaneously operating a faster rate than a pixel addressable modulator.

While the present work has yielded an order of magnitude improvement in imaging throughput; living structures exhibit dynamic behavior at all time-scales, providing ample motivation for faster systems. For studies of intracellular mass transport, an order of magnitude improvement in frame rate can be achieved with existing hardware. In recent years SLMs driven with "overdrive" control [53] have demonstrated stabilization times on the order of a few milliseconds (three times faster than in our system) and LED arrays can be used to further reduce exposure time. While in this work, the phase shifts are stepped, so that the modulator is allowed to completely settle before acquiring the frame, in principle, with the correct synchronization, it is possible to simultaneously modulate the phase and camera shutter. The primary obstacle to this kind of "bucket" integration scheme is the lack of input trigger ports on the reflection SLMs used in this work. Additionally, by switching to a three- or two-pattern phase retrieval method, a

system could combine these advances to acquire phase maps at over a hundred frames second. Such a system could then be integrated directly inside the objective

Nevertheless, the scanning of pathology slides is not limited by the speed of the modulation, but rather by the speed of the stage. This provides motivation for more creative solutions. Slide scanning would most benefit from a "time delay and integration" (TDI) approach [121], where columns of line-scan CCD elements are synchronized with the motion of the flatbed scanner's arm. Perhaps, a single-shot system like DPM could be used for this purpose. Alternatively, the TDI scanner heads can be equipped with phase shearing interferometers at fixed phase offsets, similar to a 1D version of GLIM. An unimaginative implementation of SLIM might use four phase contrast objectives.

Object recovery from phase maps, solving the inverse problem, is an outstanding challenge [70, 99]. Existing systems must compromise between sensitivity to fine detail such as nucleoli and low spatial frequency structures such as the cytosol filling a cell. Our systems have been optimized for the former. Unfortunately, many *in-vivo* structures, such as acute brain slices, show biologically relevant structures at all observable spatial scales. Thus, they contain broad frequency coverage, and cannot be segregated into relevant and irrelevant frequency components. Although typical approaches are to incrementally improve upon systems with low-frequency coverage (laser systems), we believe a more interesting approach is to improve low-frequency coverage in systems with superior high-frequency fidelity. For example, systems like white light DPM suffer from coherence artifacts [69] which may be fixed by using a defocused reference field. A method that resemble structured illumination may prove fruitful where co-localized images are acquired at different degrees of coherence. One could imagine a mechanized condenser acquiring images for different pinhole configurations [103], or a moving spiral similar to spinning disk confocal. For a ring illumination geometry, the phase ring can be made extremely narrow, increasing the spatial coherence. Images acquired at different condenser NAs can then be merged by inverting the complete, non-linear, model for partially coherent illumination image formation [69, 122, 123], rather than using a linear systems approach. By digitally apodizing the condenser function (*e.g.* a 128x128 pixel

window), this kind of nonlinear image deconvolution model can be applied in such a way that the kernel

is allowed to vary spatially where each pixel experiences a slightly different reference field perturbation.

REFERENCES

[1]   F. Zernike, "How I Discovered Phase Contrast," (in English), *Science,* vol. 121, no. 3141, pp. 345-349, 1955-03-11 00:00:00 1955.

[2]   R. D. Allen, G. B. David, and G. Nomarski, "The zeiss-Nomarski differential interference equipment for transmitted-light microscopy," (in eng), *Z Wiss Mikrosk,* vol. 69, no. 4, pp. 193-221, Nov 1969.

[3]   G. Popescu, Y. Park, W. Choi, R. R. Dasari, M. S. Feld, and K. Badizadegan, "Imaging red blood cell dynamics by quantitative phase microscopy," *Blood Cells Mol Dis,* vol. 41, no. 1, pp. 10-6, Jul-Aug 2008.

[4]   M. Mir, Z. Wang, K. Tangella, and G. Popescu, "Diffraction Phase Cytometry: blood on a CD-ROM," (in English), *Opt Express,* Article vol. 17, no. 4, pp. 2579-85, Feb 16 2009.

[5]   M. Mir, K. Tangella, and G. Popescu, "Blood testing at the single cell level using quantitative phase and amplitude microscopy," (in English), *Biomedical Optics Express,* Article vol. 2, no. 12, pp. 3259-3266, Dec 1 2011.

[6]   D. S. Mehta and V. Srivastava, "Quantitative phase imaging of human red blood cells using phase-shifting white light interference microscopy with colour fringe analysis," (in English), *Applied Physics Letters,* Article vol. 101, no. 20, p. 5, Nov 12 2012, Art. no. 203701.

[7]   H. V. Pham, B. Bhaduri, K. Tangella, C. Best-Popescu, and G. Popescu, "Real Time Blood Testing Using Quantitative Phase Imaging," (in English), *Plos One,* vol. 8, no. 2, p. e55676, Feb 6 2013.

[8]   H. Park *et al.*, "Characterizations of individual mouse red blood cells parasitized by Babesia microti using 3-D holographic microscopy," (in English), *Sci Rep,* Article vol. 5, p. 10827, Jun 03 2015, Art. no. 10827.

[9]   G. Popescu *et al.*, "Optical measurement of cell membrane tension," *Phys Rev Lett,* vol. 97, no. 21, p. 218101, Nov 24 2006.

[10]   F. Charriere *et al.*, "Cell refractive index tomography by digital holographic microscopy," *Opt Lett,* vol. 31, no. 2, pp. 178-80, Jan 15 2006.

[11]   C. Fang-Yen *et al.*, "Imaging voltage-dependent cell motions with heterodyne Mach-Zehnder phase microscopy," (in English), *Opt Lett,* Article vol. 32, no. 11, pp. 1572-4, Jun 01 2007.

[12]   W. Choi *et al.*, "Tomographic phase microscopy," *Nat Methods,* 10.1038/nmeth1078 vol. 4, no. 9, pp. 717-9, Sep 2007.

[13]   R. Wang, Z. Wang, L. Millet, M. U. Gillette, A. J. Levine, and G. Popescu, "Dispersion-relation phase spectroscopy of intracellular transport," *Opt Express,* vol. 19, no. 21, pp. 20571-9, Oct 10 2011.

[14]   W. Ru *et al.*, "One-dimensional deterministic transport in neurons measured by dispersion-relation phase spectroscopy," *Journal of Physics: Condensed Matter,* vol. 23, no. 37, p. 374107, 2011.

[15]   K. Lee *et al.*, "Quantitative phase imaging techniques for the study of cell pathophysiology: from principles to applications," *Sensors (Basel),* vol. 13, no. 4, pp. 4170-91, Mar 28 2013.

[16]   V. Tychinsky, A. V. Kretushev, I. V. Klemyashov, V. D. Zverzhkhovskiy, T. V. Vyshenskaya, and A. A. Shtil, "Quantitative phase imaging of living cells: application of the phase volume and area functions to the analysis of "nucleolar stress"," (in English), *J Biomed Opt,* Article vol. 18, no. 11, p. 111413, Nov 2013, Art. no. 111413.

[17]   T. Kim *et al.*, "White-light diffraction tomography of unlabelled live cells," (in English), *Nature Photonics,* Article vol. 8, no. 3, pp. 256-263, Mar 2014.

[18]   P. Bon, S. Lecart, E. Fort, and S. Leveque-Fort, "Fast label-free cytoskeletal network imaging in living mammalian cells," (in English), *Biophys J,* Article vol. 106, no. 8, pp. 1588-95, Apr 15 2014.

[19]   Y. Jo *et al.*, "Angle-resolved light scattering of individual rod-shaped bacteria based on Fourier transform light scattering," (in English), *Sci Rep,* Article vol. 4, p. 5090, May 28 2014, Art. no. 5090.

[20]   S. J. Gardner, N. White, J. Albon, C. Knupp, C. S. Kamma-Lorger, and K. M. Meek, "Measuring the Refractive Index of Bovine Corneal Stromal Cells Using Quantitative Phase Imaging," (in English), *Biophys J,* Article vol. 109, no. 8, pp. 1592-9, Oct 20 2015.

[21]   L. Strbkova, A. Manakhov, L. Zajickova, A. Stoica, P. Vesely, and R. Chmelik, "The adhesion of normal human dermal fibroblasts to the cyclopropylamine plasma polymers studied by holographic microscopy," (in English), *Surface & Coatings Technology,* Article; Proceedings Paper vol. 295, pp. 70-77, Jun 15 2016.

[22]   G. A. D. a. D. Zicha, *Using DRIMAPS system of transmission interference microscopy to study cell behavior, in Cell biology: a laboratory handbook*, 2 ed. 1997.

[23]   C. L. Curl *et al.*, "Quantitative phase microscopy: a new tool for measurement of cell culture growth and confluency in situ," (in English), *Pflugers Arch,* Article vol. 448, no. 4, pp. 462-8, Jul 2004.

[24]   M. Mir *et al.*, "Optical measurement of cycle-dependent cell growth," *Proc Natl Acad Sci U S A,* vol. 108, no. 32, pp. 13124-9, Aug 09 2011.

[25]   D. Bettenworth *et al.*, "Quantification of Inflammation in Colonic Tissue Sections and Wound Healing In-Vitro with Digital Holographic Microscopy," in *Advanced Microscopy Techniques Iii*, vol. 8797, E. Beaurepaire and P. T. C. So, Eds. (Proceedings of SPIE, Bellingham: Spie-Int Soc Optical Engineering, 2013.

[26]   G. Zheng, R. Horstmeyer, and C. Yang, "Wide-field, high-resolution Fourier ptychographic microscopy," *Nat Photonics,* Article vol. 7, no. 9, pp. 739-745, Sep 01 2013.

[27]   M. Mir, A. Bergamaschi, B. S. Katzenellenbogen, and G. Popescu, "Highly sensitive quantitative imaging for monitoring single cancer cell growth kinetics and drug response," *PLoS One,* vol. 9, no. 2, p. e89000, 2014.

[28]   T. A. Zangle and M. A. Teitell, "Live-cell mass profiling: an emerging approach in quantitative biophysics," *Nat Methods,* Perspective vol. 11, no. 12, pp. 1221-8, Dec 2014.

[29]   N. A. Turko, I. Barnea, O. Blum, R. Korenstein, and N. T. Shaked, "Detection and controlled depletion of cancer cells using photothermal phase microscopy," (in English), *J Biophotonics,* Article vol. 8, no. 9, pp. 755-63, Sep 2015.

[30]   L. Yu *et al.*, "Digital holographic microscopy for quantitative cell dynamic evaluation during laser microsurgery," (in English), *Opt Express,* Article vol. 17, no. 14, pp. 12031-8, Jul 06 2009.

[31]   P. Wang, R. Bista, R. Bhargava, R. E. Brand, and Y. Liu, "Spatial-domain low-coherence quantitative phase microscopy for cancer diagnosis," (in English), *Optics Letters,* Article vol. 35, no. 17, pp. 2840-2842, Sep 2010.

[32]   Z. Wang, K. Tangella, A. Balla, and G. Popescu, "Tissue refractive index as marker of disease," (in English), *J Biomed Opt,* vol. 16, no. 11, p. 116017, Nov 2011.

[33]   T. Kim, S. Sridharan, A. Kajdacsy-Balla, K. Tangella, and G. Popescu, "Gradient field microscopy for label-free diagnosis of human biopsies [Invited]," *Appl Opt,* vol. 52, no. 1, pp. A92-6, Jan 01 2013.

[34]   H. V. Pham, L. Pantanowitz, and Y. Liu, "Quantitative phase imaging to improve the diagnostic accuracy of urine cytology," *Cancer Cytopathol,* vol. 124, no. 9, pp. 641-50, Sep 2016.

[35]   S. Sridharan *et al.*, "Prediction of prostate cancer recurrence using quantitative phase imaging: Validation on a general population," *Sci Rep,* vol. 6, p. 33818, Sep 23 2016.

[36]   B. Bhaduri, M. Kandel, C. Brugnara, K. Tangella, and G. Popescu, "Optical assay of erythrocyte function in banked blood," *Sci Rep,* Article vol. 4, p. 6211, Sep 05 2014.

[37]   S. Ceballos, M. Kandel, S. Sridharan, H. Majeed, F. Monroy, and G. Popescu, "Active intracellular transport in metastatic cells studied by spatial light interference microscopy," *J Biomed Opt,* vol. 20, no. 11, p. 111209, 2015.

[38]   M. Kandel, K. W. Teng, P. R. Selvin, and G. Popescu, "Highly sensitive kinesin-microtubule motility assays using SLIM," 2016, vol. 9718, pp. 97180T-97180T-5.

[39]   H. Majeed *et al.*, "Diagnosis of breast cancer biopsies using quantitative phase imaging," 2015, vol. 9336, pp. 93361R-93361R-6.

[40]   H. Majeed *et al.*, "Breast cancer diagnosis using spatial light interference microscopy," (in English), *Journal of Biomedical Optics,* vol. 20, no. 11, pp. 111210-111210, Nov 2015.

[41]   H. Majeed *et al.*, "Automatic tissue segmentation of breast biopsies imaged by QPI," 2016, vol. 9718, pp. 971817-971817-6.

[42]   H. Majeed *et al.*, "High throughput imaging of blood smears using white light diffraction phase microscopy," 2016, vol. 9336, pp. 93361Y-93361Y-5.

[43]   M. Kandel *et al.*, "Label-free tissue scanner for colorectal cancer screening (under review)," 2016.

[44]   G. Magyar and L. Mandel, "Interference Fringes Produced by Superposition of Two Independent Maser Light Beams," *Nature,* 10.1038/198255a0 vol. 198, no. 4877, pp. 255-256, 04/20/print 1963.

[45]   A. H. Fischer, K. A. Jacobson, J. Rose, and R. Zeller, "Hematoxylin and eosin staining of tissue and cell sections," *CSH Protoc,* vol. 2008, no. 5, p. pdb prot4986, May 01 2008.

[46]   A. M. Zysk, R. W. Schoonover, P. S. Carney, and M. A. Anastasio, "Transport of intensity and spectrum for partially coherent fields," *Opt Lett,* vol. 35, no. 13, pp. 2239-41, Jul 01 2010.

[47]   A. F. Huxley and R. Niedergerke, "Structural changes in muscle during contraction; interference microscopy of living muscle fibres," *Nature,* 10.1038/173971a0 vol. 173, no. 4412, pp. 971-3, May 22 1954.

[48]   H. G. Davies, M. H. F. Wilkins, J. Chayen, and L. F. Lacour, "The Use of the Interference Microscope to Determine Dry Mass in Living Cells and as a Quantitative Cytochemical Method," (in English), *Quarterly Journal of Microscopical Science,* vol. 95, no. 3, pp. 271-&, 1954.

[49]   M. Loehrer *et al.*, "In vivo assessment by Mach-Zehnder double-beam interferometry of the invasive force exerted by the Asian soybean rust fungus (Phakopsora pachyrhizi)," *New Phytol,* vol. 203, no. 2, pp. 620-31, Jul 2014.

[50]   P. de Groot, "Principles of interference microscopy for the measurement of surface topography," *Advances in Optics and Photonics,* vol. 7, no. 1, p. 1, 2015/03/31 2015.

[51]   S. Mallick and D. Malacara, "Common-Path Interferometers," in *Optical Shop Testing*: John Wiley & Sons, Inc., 2006, pp. 97-121.

[52]   D. Malacara, "Optical Shop Testing (Wiley Series in Pure and Applied Optics)," Wiley-Interscience, 2007.

[53]   T. H. Nguyen and G. Popescu, "Spatial Light Interference Microscopy (SLIM) using twisted-nematic liquid-crystal modulation," *Biomed Opt Express,* vol. 4, no. 9, pp. 1571-83, 07/30/ 2013.

[54]   G. Popescu, T. Ikeda, R. R. Dasari, and M. S. Feld, "Diffraction phase microscopy for quantifying cell structure and dynamics," *Opt Lett,* vol. 31, no. 6, pp. 775-7, Mar 15 2006.

[55]   T. H. Nguyen, C. Edwards, L. L. Goddard, and G. Popescu, "Quantitative phase imaging with partially coherent illumination," *Opt Lett,* vol. 39, no. 19, pp. 5511-4, Oct 01 2014.

[56]   M. Shan, M. Kandel, H. Majeed, V. Nastasa, and P. Gabriel, "White-light diffraction phase microscopy at full space-bandwidth product (in press)," *Optics Express,* 2016.

[57]   B. Bhaduri *et al.*, "Diffraction phase microscopy: principles and applications in materials and life sciences," (in English), *Advances in Optics and Photonics,* vol. 6, no. 1, pp. 57-119, Mar 2014.

[58]   N. T. Shaked, Y. Zhu, M. T. Rinehart, and A. Wax, "Two-step-only phase-shifting interferometry with optimized detector bandwidth for microscopy of live cells," *Opt Express,* vol. 17, no. 18, pp. 15585-91, Aug 31 2009.

[59]   H. Kadono, N. Takai, and T. Asakura, "New common-path phase shifting interferometer using a polarization technique," *Appl Opt,* vol. 26, no. 5, pp. 898-904, Mar 01 1987.

[60]   H. Kadono, M. Ogusu, and S. Toyooka, "Phase-Shifting Common-Path Interferometer Using a Liquid-Crystal Phase Modulator," (in English), *Optics Communications,* vol. 110, no. 3-4, pp. 391-400, Aug 15 1994.

[61]   M. E. Kandel, K. W. Teng, P. R. Selvin, and P. Gabriel, "Label-free imaging of single microtubule dynamics using spatial light interference microscopy (SLIM) (accepted)," *ACS Nano,* 2016.

[62]   M. E. Kandel, M. Rubessa, D. Fernandes, T. H. Nguyen, M. B. Wheeler, and G. Popescu, "Monitoring in-vitro bovine embryo development during the first days after fertilization (Conference Presentation)," 2016, vol. 9718, pp. 97180M-97180M-1.

[63]   M. Kandel, T. Nguyen, and P. Gabriel, "Label-free tomographic reconstruction of optically thick structures using GLIM," in *Quantitative Phase Imaging III*, 2017.

[64]   J. Mertz, *Introduction to Optical Microscopy*. W. H. Freeman, 2009.

[65]   Z. Wang *et al.*, "Spatial light interference tomography (SLIT)," *Opt Express,* vol. 19, no. 21, pp. 19907-18, Oct 10 2011.

[66]   C. Edwards, A. Arbabi, G. Popescu, and L. L. Goddard, "Optically monitoring and controlling nanoscale topography during semiconductor etching," *Light Sci Appl,* vol. 1, p. e30, 09/28/online 2012.

[67]   R. Zhou, C. Edwards, A. Arbabi, G. Popescu, and L. L. Goddard, "Detecting 20 nm Wide Defects in Large Area Nanopatterns Using Optical Interferometric Microscopy," *Nano Letters,* vol. 13, no. 8, pp. 3716-3721, 2013/08/14 2013.

[68]   G. Rajshekhar, B. Bhaduri, C. Edwards, R. Zhou, L. L. Goddard, and G. Popescu, "Nanoscale topography and spatial light modulator characterization using wide-field quantitative phase imaging," *Optics Express,* vol. 22, no. 3, pp. 3432-3438, 2014/02/10 2014.

[69]   C. Edwards *et al.*, "Effects of spatial coherence in diffraction phase microscopy," *Opt Express,* vol. 22, no. 5, pp. 5133-46, Mar 10 2014.

[70]   G. Thalhammer, R. W. Bowman, G. D. Love, M. J. Padgett, and M. Ritsch-Marte, "Speeding up liquid crystal SLMs using overdrive with phase change reduction," *Opt Express,* vol. 21, no. 2, pp. 1779-97, Jan 28 2013.

[71]   M. Kirschner and T. Mitchison, "Beyond self-assembly: from microtubules to morphogenesis," (in English), *Cell,* vol. 45, no. 3, pp. 329-42, May 09 1986.

[72]   J. V. Small, B. Geiger, I. Kaverina, and A. Bershadsky, "How do microtubules guide migrating cells?," (in English), *Nat Rev Mol Cell Biol,* vol. 3, no. 12, pp. 957-64, Dec 2002.

[73]   P. J. de Pablo, I. A. Schaap, F. C. MacKintosh, and C. F. Schmidt, "Deformation and collapse of microtubules on the nanometer scale," (in English), *Phys Rev Lett,* vol. 91, no. 9, p. 098101, Aug 29 2003.

[74]   A. Akhmanova and M. Dogterom, "Kinesins lead aging microtubules to catastrophe," *Cell,* vol. 147, no. 5, pp. 966-8, Nov 23 2011.

[75]   T. Vicsek, "Biological physics: Swarming microtubules," *Nature,* vol. 483, no. 7390, pp. 411-2, Mar 21 2012.

[76]   J. Brugues, V. Nuzzo, E. Mazur, and D. J. Needleman, "Nucleation and transport organize microtubules in metaphase spindles," *Cell,* vol. 149, no. 3, pp. 554-64, Apr 27 2012.

[77] H. Kadavath *et al.*, "Tau stabilizes microtubules by binding at the interface between tubulin heterodimers," *Proc Natl Acad Sci U S A,* vol. 112, no. 24, pp. 7501-6, Jun 16 2015.

[78] J. Schaletzky and M. Rape, "Getting a Grip on Microtubules," *Cell,* vol. 164, no. 5, pp. 836-7, Feb 25 2016.

[79] R. D. Vale, "The molecular motor toolbox for intracellular transport," *Cell,* vol. 112, no. 4, pp. 467-80, Feb 21 2003.

[80] R. Mohan *et al.*, "End-binding proteins sensitize microtubules to the action of microtubule-targeting agents," *Proc Natl Acad Sci U S A,* vol. 110, no. 22, pp. 8900-5, May 28 2013.

[81] I. M. Kulic *et al.*, "The role of microtubule movement in bidirectional organelle transport," (in English), *Proc Natl Acad Sci U S A,* vol. 105, no. 29, pp. 10011-6, Jul 22 2008.

[82] M. A. Jordan and L. Wilson, "Microtubules and actin filaments: dynamic targets for cancer chemotherapy," *Curr Opin Cell Biol,* vol. 10, no. 1, pp. 123-30, Feb 1998.

[83] R. D. Allen, N. S. Allen, and J. L. Travis, "Video-enhanced contrast, differential interference contrast (AVEC-DIC) microscopy: a new method capable of analyzing microtubule-related motility in the reticulopodial network of Allogromia laticollaris," *Cell Motil,* vol. 1, no. 3, pp. 291-302, 1981.

[84] T. Horio and H. Hotani, "Visualization of the dynamic instability of individual microtubules by dark-field microscopy," *Nature,* 10.1038/321605a0 vol. 321, no. 6070, pp. 605-7, Jun 5-11 1986.

[85] M. Goedert, M. G. Spillantini, R. Jakes, D. Rutherford, and R. A. Crowther, "Multiple isoforms of human microtubule-associated protein tau: sequences and localization in neurofibrillary tangles of Alzheimer's disease," *Neuron,* vol. 3, no. 4, pp. 519-26, Oct 1989.

[86] M. Bailey, L. Conway, M. W. Gramlich, T. L. Hawkins, and J. L. Ross, "Modern methods to interrogate microtubule dynamics," *Integr Biol (Camb),* 10.1039/C3IB40124C vol. 5, no. 11, pp. 1324-33, Nov 2013.

[87] J. Walter. (2007). *FFT Filter*. Available: http://rsb.info.nih.gov/ij/plugins/fft-filter.html

[88] F. D. Lewis, "Sorting Networks," Available: http://cs.engr.uky.edu/~lewis/essays/algorithms/sortnets/sort-net.html

[89] J. Andrecka, J. Ortega Arroyo, K. Lewis, R. A. Cross, and P. Kukura, "Label-free Imaging of Microtubules with Sub-nm Precision Using Interferometric Scattering Microscopy," *Biophys J,* vol. 110, no. 1, pp. 214-7, Jan 05 2016.

[90] N. A. Reed *et al.*, "Microtubule acetylation promotes kinesin-1 binding and transport," *Curr Biol,* vol. 16, no. 21, pp. 2166-72, Nov 07 2006.

[91] M. Mir *et al.*, "Label-free characterization of emerging human neuronal networks," *Sci Rep,* Article vol. 4, p. 4434, Mar 24 2014.

[92] NIH, "Follow that Cell: Single Cell Analysis Program," ed, 2014.

[93] M. Kandel, J. Liang, and G. Popescu, "Emergent patterns in cellular growth as studied by QPI," in *SPIE Photonics West: BiOS*, San Francisco, CA, 2015.

[94] G. Popescu *et al.*, "Optical imaging of cell mass and growth dynamics," *Am J Physiol Cell Physiol,* vol. 295, no. 2, pp. C538-44, Aug 2008.

[95] C. Smith. (2012, 11/5/2016). *Cell Proliferation Assays: Methods for Measuring Dividing Cells*. Available: http://www.biocompare.com/Editorial-Articles/117892-Cell-Proliferation-Assays/

[96] E. C. Anderson, G. I. Bell, D. F. Petersen, and R. A. Tobey, "Cell growth and division. IV. Determination of volume growth rate and division probability," *Biophys J,* vol. 9, no. 2, pp. 246-63, Feb 1969.

[97] B. Huang, S. A. Jones, B. Brandenburg, and X. W. Zhuang, "Whole-cell 3D STORM reveals interactions between cellular structures with nanometer-scale resolution," (in English), *Nature Methods,* 10.1038/nmeth.1274 vol. 5, no. 12, pp. 1047-1052, Dec 2008.

[98]   E. Meijering, O. Dzyubachyk, and I. Smal, "Chapter nine - Methods for Cell and Particle Tracking," in *Methods in Enzymology*, vol. Volume 504, P. M. conn, Ed.: Academic Press, 2012, pp. 183-200.

[99]   F. Macias-Garza, A. C. Bovik, K. R. Diller, S. J. Aggarwal, and J. K. Aggarwal, "The missing cone problem and low-pass distortion in optical serial sectioning microscopy," in *Acoustics, Speech, and Signal Processing, 1988. ICASSP-88., 1988 International Conference on*, 1988, pp. 890-893 vol.2.

[100]   M. Mir, S. D. Babacan, M. Bednarz, M. N. Do, I. Golding, and G. Popescu, "Visualizing Escherichia coli sub-cellular structure using sparse deconvolution Spatial Light Interference Tomography," *PLoS One,* vol. 7, no. 6, p. e39816, 2012.

[101]   R. L. Breckenridge, R. L. Rehermann, and E. T. Gibson, "Congenital cystic adenomatoid malformation of the lung," *J Pediatr,* Article vol. 67, no. 5, pp. 863-6, Nov 1965.

[102]   A. Griffa, N. Garin, and D. Sage, "Comparison of Deconvolution Software: A User Point of View—Part 2," *G.I.T. Imaging & Microscopy,* vol. 12, no. 3, pp. 41–43, 2010.

[103]   J. Lim *et al.*, "Comparative study of iterative reconstruction algorithms for missing cone problems in optical diffraction tomography," *Opt Express,* vol. 23, no. 13, pp. 16933-48, Jun 29 2015.

[104]   J. G. McNally, T. Karpova, J. Cooper, and J. A. Conchello, "Three-dimensional imaging by deconvolution microscopy," *Methods,* vol. 19, no. 3, pp. 373-85, Nov 1999.

[105]   M. Habaza, B. Gilboa, Y. Roichman, and N. T. Shaked, "Tomographic phase microscopy with 180 degrees rotation of live cells in suspension by holographic optical tweezers," *Opt Lett,* vol. 40, no. 8, pp. 1881-4, Apr 15 2015.

[106]   V. Lucic, F. Forster, and W. Baumeister, "Structural studies by electron tomography: from cells to molecules," *Annu Rev Biochem,* vol. 74, no. 1, pp. 833-65, 2005.

[107]   Y. Sung, W. Choi, N. Lue, R. R. Dasari, and Z. Yaqoob, "Stain-free quantification of chromosomes in live cells using regularized tomographic phase microscopy," *PLoS One,* vol. 7, no. 11, p. e49502, 2012.

[108]   W. R. Zipfel, R. M. Williams, and W. W. Webb, "Nonlinear magic: multiphoton microscopy in the biosciences," *Nat Biotechnol,* 10.1038/nbt899 vol. 21, no. 11, pp. 1369-77, Nov 2003.

[109]   E. W. Max Born, "Principles of Optics Electromagnetic Theory of Propagation, Interference and Diffraction of Light," 7 ed., 1999.

[110]   G. Strang, "The Discrete Cosine Transform," *SIAM Review,* vol. 41, no. 1, pp. 135-147, 1999/01/01 1999.

[111]   E. Tuck and V. Cavalli, "Roles of membrane trafficking in nerve repair and regeneration," *Commun Integr Biol,* vol. 3, no. 3, pp. 209-14, May 2010.

[112]   O. E. Bloom and J. R. Morgan, "Membrane trafficking events underlying axon repair, growth, and regeneration," *Mol Cell Neurosci,* vol. 48, no. 4, pp. 339-48, Dec 2011.

[113]   M. E. Kandel, H. Shakir, D. Fernandes, C. Best, and G. Popescu, "Helmholtz Equation Approach to 4D Label-free Imaging of Neuron Transport (in prep.)," 2016.

[114]   T. H. Nguyen, M. E. Kandel, and G. Popescu, "Gradient light interference microscopy (GLIM) for imaging thick specimens " in *Quantitative Phase Imaging II*, 2016: SPIE.

[115]   M. Barisic *et al.*, "Mitosis. Microtubule detyrosination guides chromosomes during mitosis," *Science,* vol. 348, no. 6236, pp. 799-803, May 15 2015.

[116]   J. Kiefer, "Sequential Minimax Search for a Maximum," (in English), *Proceedings of the American Mathematical Society,* vol. 4, no. 3, pp. 502-506, 1953.

[117]   A. Haar, "Zur Theorie der orthogonalen Funktionensysteme," (in German), *Mathematische Annalen,* vol. 69, no. 3, pp. 331-371, 1910/09/01 1910.

[118]   S. Mallat and S. Zhong, "Characterization of Signals from Multiscale Edges," (in English), *Ieee Transactions on Pattern Analysis and Machine Intelligence,* vol. 14, no. 7, pp. 710-732, Jul 1992.

[119]   E. De Castro and C. Morandi, "Registration of Translated and Rotated Images Using Finite Fourier Transforms," *IEEE Transactions on Pattern Analysis and Machine Intelligence,* vol. PAMI-9, no. 5, pp. 700-703, 1987.

[120]   M. Shan, M. Kandel, and P. Gabriel, "Refractive index variance of cells and tissues measured by quantitative phase imaging (in press)," *Opt Express,* 2016.

[121]   D. Barbe, "Time delay and integration image sensors," *Solid state imaging,* vol. 659, 1976.

[122]   T. H. Nguyen, H. Majeed, C. A. Edwards, M. N. Do, L. L. Goddard, and G. Popescu, "Halo-free quantitative phase imaging with partially coherent light," 2015, vol. 9336, pp. 93360N-93360N-5.

[123]   T. Nguyen *et al.*, "Halo-free Phase Contrast Microscopy (under review)," 2016.